1  **Plio-Pleistocene ocean circulation changes in the GOA and its impacts on the**
2  **carbon and nitrogen cycles and the CIS development.**

3  **Maria Luisa Sánchez Montes[1,2], Oscar E. Romero[3,4], Ellen A. Cowan[5], Juliane Müller[3,4],**
4  **Christopher M. Moy[6], Jeremy M. Lloyd[1] and Erin L. McClymont[1]**

5  [1] Department of Geography, Durham University, Durham, UK.

6  [2] School of Environmental Sciences, University of East Anglia, Norwich, UK.

7  [3] MARUM – Center for Marine Environmental Sciences, University of Bremen, Bremen,
8  Germany.

9  [4] Alfred Wegener Institute Helmholtz Centre for Polar and Marine Research, Bremerhaven,
10  Germany.

11  [5] Department of Geological and Environmental Sciences, Appalachian State University, North
12  Carolina, USA.

13  [6] Department of Geology, University of Otago, Dunedin, New Zealand.

14  Corresponding author: Maria Luisa Sánchez Montes (m.sanchez-montes@uea.ac.uk)

15  **Key Points:**

16  • The Cordilleran Ice Sheet expansion created high nutrient low chlorophyll conditions.

17  • Biogeochemical changes in the Gulf of Alaska follow 400 and 100 kyr eccentricity
18   cycles.

19  • Increased marine productivity export contributed to the atmospheric $CO_2$ drawdown
20   and further Cordilleran Ice Sheet expansion.

21  **Abstract**

22  The modern Gulf of Alaska (GOA) is a high nutrient low chlorophyll (HNLC) region,
23  estimated to be important for nutrient cycling and $CO_2$ exchange. Little is known of the GOA
24  evolution over the Pliocene and Pleistocene as well as its impact on the Cordilleran Ice Sheet
25  (CIS) development, when other evidence for changing North Pacific circulation has emerged.
26  We analysed IODP Expedition 341 Site U1417 sediments, which extend through the Plio-
27  Pleistocene transition (4-1.7 Ma), focussing on productivity-related biomarkers (alkenones,
28  brassicasterol), siliceous microfossils and bulk carbon and nitrogen stable isotopes. Our results
29  show two dominant water column regimes: one characterised by high silica and low organic
30  matter preservation, containing microorganism remains from a mix of habitats (4-3.7 Ma) and
31  a second characterised by low biogenic silica and increased organic matter preservation of
32  microorganisms from dominantly open ocean habitats (3.33-3.32 Ma and 2.8-1.66 Ma). An
33  increase of phytoplankton diversity (3.7-3.35 Ma, 3.19-2.82 Ma) characterises the two
34  transitions of water column conditions, from oxygenated to reductive, that we attribute to a
35  change from ocean mixing to strong stratified conditions with some occasional mixing. The
36  biogeochemical changes in the GOA follow 400 and 100 kyr eccentricity cycles which are also
37  reflected in changes in the CIS. We conclude that the CIS expansion created HNLC conditions
38  in the GOA during the Mid Piacenzian Warm Period (MPWP) and the early Pleistocene. In

39 turn, positive feedbacks increased marine productivity export, atmospheric $CO_2$ drawdown and
40 further CIS expansion.

**1 Introduction**

42 During the Pliocene and Pleistocene transition (PPT) and intensification of the Northern
43 Hemisphere Glaciation (iNHG, ~2.6 Ma), changes to marine productivity export patterns have
44 been recorded by means of biogenic silica and alkenone sediment concentrations and linked to
45 changing ocean circulation. In the subarctic Pacific (Haug *et al*., 2005; Studer *et al.,* 2012),
46 Bering Sea (März *et al.*, 2013), Southern Ocean (Sigman *et al*., 2004) and parts of the North
47 Atlantic (Lawrence *et al.*, 2013; Lawrence *et al.*, 2009) marine productivity export is higher
48 before the iNHG. In contrast, other parts of the North Atlantic (Site 607; Lawrence *et al.,* 2013),
49 in the South Atlantic (Cortese *et al*., 2004; Martínez-Garcia *et al.,* 2010) and the equatorial
50 Pacific (Liu *et al*., 2008; Lawrence *et al*., 2006; Lawrence *et al*., 2013) the marine productivity
51 export is higher after the iNHG. The different patterns in marine productivity export during the
52 iNHG has been suggested to derive from changes in nutrient distribution (Etourneau *et al.,*
53 2012) and the equatorial migration of the westerly winds (Lawrence *et al.*, 2013). It has been
54 observed that higher atmospheric $CO_2$ concentrations occurred when the Southern Ocean and
55 North Pacific were well ventilated (Etourneau *et al.,* 2012) during the warm mid-Pliocene (3.5-
56 3.0 Ma). The development of polar stratification over the PPT, and the resulting limitation in
57 surface ocean macronutrient availability to fuel marine productivity, could have restricted
58 ocean-atmosphere $CO_2$ exchange in the North Pacific, impacting the climate globally (e.g.,
59 Haug *et al.,* 2005; Etourneau *et al.,* 2012). Although these changes have been observed in the
60 northwestern Pacific and Bering Sea (Haug *et al*., 2005; März *et al.*, 2013), it remains unclear
61 how marine productivity in the northeast Pacific changed over the PPT.

62 Here, we reconstruct marine productivity changes in the Gulf of Alaska (GOA), northeast
63 Pacific, through the mid- and late-Pliocene and early Pleistocene (4.0-1.7 Ma), analysing
64 sediments from the Integrated Ocean Drilling Program (IODP) Expedition 341 Site U1417
65 (Figure 1). The proximity of the GOA to the Cordilleran Ice Sheet (CIS, Figure 1), which
66 expanded over this time interval (Gulick *et al.,* 2015; Sánchez-Montes *et al.,* 2020, Huber and
67 Bahlburg, 2021), allows direct examination of how the evolution of a large ice mass affects the
68 supply of macro/micronutrients via fluvial and glacial transport to the ocean to influence
69 marine productivity (Müller *et al.,* 2018). Based on previous research (Haug *et al.,* 2005;
70 Lawrence *et al*., 2013), one hypothesis is that the marine productivity in the subarctic Pacific
71 was higher before the iNHG due to increased deep nutrient mixing. However, we have
72 previously shown that some biomarkers for marine production at Site U1417 (aquatic *n*-alkane,
73 Sánchez-Montes *et al.,* 2020) suggest an increase in marine productivity in the GOA after the
74 iNHG water column stratification, which might suggest increasing nutrient availability linked
75 to the intensification of the glaciation. It is important to differentiate between these hypotheses,
76 because marine productivity and a change in the North Pacific circulation can have an impact
77 on atmospheric $CO_2$ concentrations and shifts in climate (e.g., Williamson & Holligan, 1990).
78 Here, we examine aquatic productivity changes over iNHG using a multi-proxy approach by
79 focussing on evidence for marine productivity export through a combination of diatom
80 assemblages (i.e Katsuki *et al.,* 2003), alkenones (haptophyte algae, Marlowe *et al*., 1984),
81 brassicasterol (diatoms, Kanazawa *et al.,* 1971; haptophytes, Volkman *et al.,* 1986) aquatic *n*-
82 alkanes (algae and cyanobacteria, Bourbonniere and Meyers, 1996; Han & Calvin, 1969) and
83 both the accumulation rate and isotopic composition of nitrogen and organic carbon (Hedges
84 & Keil, 1995; Burdige, 2005, 2007; Walinsky *et al.,* 2009; Addison *et al.,* 2012). We combine
85 these approaches with evidence for inputs of terrestrial OM from dust/river/glacial sediment
86 using terrigenous *n*-alkanes (Rieley *et al*., 1991) and previously published glacier inputs (IRD

87   and %C$_{37:4}$ alkenone, Sánchez-Montes *et al.,* 2020), to assess whether changes to terrestrial
88   nutrient supply also occurred.

**2 Research Site**

90   The main GOA oceanographic features include the Alaskan Current (AC) and the Alaskan
91   Coastal Current (ACC) (Figure 1). The AC travels north along the North American west coast
92   and is sourced in warm mid-latitude currents in the North Pacific travelling eastwards around
93   45° N as the North Pacific Current (NPC). Site U1417 (56°57.58′ N, 147°6.58′ W; water depth
94   4,218 m) is currently located under the influence of the AC, characterized by iron-limited,
95   nitrate-rich, low chlorophyll waters in a High Nutrient Low Chlorophyll (HNLC) region
96   (Martin & Fitzwater, 1988; Martin *et al*., 1991; Hinckley *et al*., 2009; Figure 1). Productivity
97   in the HNLC region at the centre of the Alaska Gyre requires advection of deep, nutrient-rich
98   waters to reach the surface, which reaches a maximum when the Aleutian Low (AL) is centred
99   in the GOA during winter (Figure 1), and when micronutrients (e.g., iron) are supplied from
100  land. Alaskan glacial iron input to the GOA is aided by strong winds associated with the AL in
101  the GOA during autumn (Schroth *et al.,* 2017) but reaches a maximum during August, when
102  Alaskan glacio-fluvial sediments are exposed (Crusius *et al.,* 2011). Asian dust has also been
103  found in the St. Elias Mountains during early April storm events and increased westerly winds
104  (Zdanowicz *et al.,* 2006). Coccolithophorids and diatoms appear as the main phytoplankton
105  groups in the GOA, the former being able to cope with small iron inputs but not able to compete
106  with the latter when iron is available (Martin *et al.,* 1989). The AC later forms the Alaska
107  Stream (AS) when exiting the GOA travelling westwards. The ACC travels northwards along
108  the coast of southwest Alaska towards the Aleutian Arch and to the Bering Sea. A low nutrient
109  high chlorophyll (LNHC) regime dominates under the influence of the ACC closer to coastal
110  Alaska (Whitney *et al.,* 2005). Productivity in the LNHC region requires downwelling
111  relaxation and advection of deep nutrient rich waters for macronutrient availability (e.g.,
112  nitrate) into the surface ocean (Figure 1). The ACC is characterised by its low salinity due to
113  the incorporation of glacial and river discharge into the GOA, which is maximum during
114  summer (Figure 1). At present, meltwater is transported along the coastal GOA through the
115  ACC (Kipphut, 1990).

**3 Materials and Methods**

117  3.1 Age model, sedimentation rates and recovered sediment at Site U1417.

118  This study analysed Site U1417 sediment depths between 417.3 and 212.2 m CCSF-A dating
119  from 4.0 to 1.66 Ma. The age model and calculated sedimentation rates used in this study are
120  based on the shipboard age model (Jaeger *et al*., 2014) assuming an even distribution of the
121  recovered material between top and bottom cores when the recovery was incomplete (see
122  Sánchez-Montes *et al.,* 2020; Table S1). The shipboard age model from 1.66 and 2.2 Ma is
123  well constrained by magnetostratigraphic reversals found in U1417B or U1417D (C2n(T)
124  Olduvai top, C2n(B) Olduvai base, C2r.1n (T) Reunion top and C2r.1n (B) Reunion base) and
125  sediment recovery in this section is close to 100% (Jaeger *et al*., 2014). This section of the age
126  model remains unchanged in the modified age model used by Sánchez-Montes *et al*. (2020)
127  and the age errors adopted here from Jaeger *et al*., 2014 account to ±0.02 Ma, with a propagated
128  error across neighbouring samples of ±0.028 Ma. For the sediment record older than 2.2 Ma
129  (288.45 m) sediment recovery reduces significantly (70 to 12%; Jaeger *et al*., 2014). The
130  revised age model redistributes this material across the core sections assuming no loss in
131  material (Sánchez-Montes *et al* 2020). The age model adjustments resulted in a similar
132  age/depth of the C2r.2r (B) Gauss/Matuyama top (found in U1417B, D and E), however,
133  C2An.3n (B) Gilbert/Gauss transition found only in U1417D shifted from 408.26 to 410.75 m

134     CCSF-A and from 3.75 to 3.88 Ma (Jaeger *et al*., 2014; Sánchez-Montes *et al* 2020). While the
135     depth error remains the same, the age error over this section of the core has been increased to
136     ±0.12 Ma to take the Gilbert/Gauss transition age shift into account, with a propagated error
137     across neighbouring samples between ±0.23 to ±0.69 Ma. The are no big shifts in between the
138     sedimentation rates calculated from the age model of Jaeger *et al.,* 2014 and our stretched age
139     model, which give confidence that our proposed age model only refines the shipboard age
140     model (Sánchez-Montes *et al.,* 2020). Beyond 3.88 Ma U1417's age model is poorly
141     constrained due to poor core recovery (see Jaeger *et al.,* 2014; Sánchez-Montes *et al*., 2020)
142     and, therefore, it determines the lower age range of this study to 4 Ma.

143     Uncertainty of the age model and sedimentation rates presented here follow the polarity
144     chronozone interpretations of the shipboard age model (Jaeger *et al.,* 2014; Gulick *et al.,* 2014)
145     and accounts for shifts in the Gilbert-Gauss magnetic reversal in the adjusted age-depth model
146     (Sánchez-Montes *et al.,* 2020, Table S1). The sedimentation rates are calculated across our
147     analysed samples, almost exclusively in Hole U1417D. Sedimentation rates increase during
148     the mid and late Pliocene (from 40 to 85m/Myr across 3.5-2.8 Ma), and during the iNHG
149     increase in glaciogenic inputs (from 85 to 156 m/Myr at 2.4 Ma). Our manually calculated
150     sedimentation rates on the CCSF-A scale across neighbouring samples follow the depth-age
151     model uncertainties of Jager *et al.* (2014) but differ slightly from the shipboard age model,
152     where average sedimentation rates are calculated over 0.5 Myrs following the CCSF-B scale,
153     and uncertainties (+1σ) are calculated using a Monte-Carlo sedimentation model over the
154     whole Site U1417 (Jaeger *et al.,* 2014). After distributing the sediment evenly across the core
155     (Sánchez-Montes *et al.,* 2020), our calculated sedimentation rate uncertainties become smaller
156     when compared to the statistical approach of the shipboard age model (Jaeger *et al.,* 2014). The
157     sediments recovered include diatom ooze interbedded with debris flow deposits containing
158     mud clasts and plant fragments (lithostratigraphic unit VA, 4-3.2 Ma), marine mud (unit IV
159     and II, 3.2-2.8 Ma and 2.4-1.66 Ma) and ice-rafted diamict interbedded with mud (unit III, 2.8-
160     2.4 Ma; Jaeger *et al*., 2014). Samples for organic matter analyses were selected avoiding sand,
161     silt, ash or gravel (e.g. Ausín *et al*., 2019, 2021).

162     3.2 Carbon and nitrogen bulk and isotope analyses.

163     Approximately 70 mg of freeze-dried and homogenized sediment was weighed into silver
164     capsules and acidified in-situ with 5-6% sulphurous acid ($H_2SO_3$) to remove carbonate phases
165     (Verardo *et al*., 1990). Additional aliquots of acid were repeated until no reaction was observed
166     using a binocular microscope, which ensured removal of inorganic carbon. No method was
167     implemented for inorganic nitrogen removal. Samples were oven-dried between acidifications
168     at 40 °C. 6 mg of Tungsten VI oxide ($WO_3$) was added to each sample to facilitate combustion.
169     Samples were then measured using a Varian elemental analyser coupled to a Europa Scientific
170     continuous-flow isotope-ratio mass spectrometer. The average standard deviation of replicate
171     samples is 0.58 ‰ for $\delta^{15}N$, 0.006 % for total nitrogen (TN), 0.26 ‰ for $\delta^{13}C$ and 0.031% for
172     total organic carbon (TOC) (n = 8 pairs). The TOC and TN were normalised to the
173     accumulation rates of the sediment analysed (Equation 1-3), where "material" refers to TOC
174     or TN:

175     **Equation 1:** $\text{Material (mg g}^{-1}) = \frac{\text{Mass material (mg)}}{\text{Weight sample (g)}}$

176     **Equation 2:** $\text{Bulk MAR (g cm}^{-2}\text{kyr}^{-1}) = \frac{\text{Dry bulk density (g cm}^{-3})}{\text{Sedimentation rates (cm kyr}^{-1})}$

177     **Equation 3:** $\text{Material MAR} = \text{Bulk MAR} * \text{Material}$

178     3.3 Siliceous microfossil assemblages and biogenic silica.

179  Microplaeontological counting standard methods and techniques (Schrader & Gersonde, 1978)
180  were followed to prepare sediments after freeze-drying. Siliceous microfossil species
181  identification and counts were performed on pre-acid cleaned permanent slides (*Mountex*®
182  mounting medium). Several traverses across each slide were examined on a *Zeiss*®Axioscop
183  with interference illumination at x1000 magnifications (MARUM, University of Bremen).
184  Depending on valve abundances, between ca. 400 and ca. 700 valves per slide were counted.
185  Duplicate slide counting quantified the concentration estimate analytical error ≤10.0 %.
186  Counting outputs were converted in sedimentary abundance of individual diatom taxa, total
187  diatom (in valves per $g^{-2}$) and total silicoflagellate (in skeletons per $g^{-2}$, Equation 4) which were
188  then converted to mass accumulation rates (MAR, Equation 3). The relative abundance (%) of
189  each species was calculated as the fraction of the diatom species versus the TC in a particular
190  sample (Equation 4).

191  **Equation 4:** $TC = [N] \left[\frac{A}{a}\right] \left[\frac{1}{W}\right] \left[\frac{V}{v}\right]$

192  where, TC is the total concentration, [N] is the number of valves in [a], an known area, [A] is
193  the total area of a petri dish, [W] the sample weight in grams, and [V/v] the sample volume of
194  the permanent slide (Sancetta & Calvert, 1988).

195  Diatom taxa were grouped in 6 palaeo-habitats: benthic, coastal high productivity, coastal
196  moderate productivity, pelagic high productivity, pelagic warm water and freshwater (Table
197  S2). The coastal high and moderate productivity palaeo-habitats describe coastal diatoms that
198  occur at intervals of high and moderate productivity due to high and moderate nutrient
199  availability in surface coastal waters, respectively. The pelagic high productivity palaeo-habitat
200  is composed by pelagic diatoms that occur at intervals of high productivity and high nutrient
201  availability in surface pelagic waters. The pelagic warm waters is a palaeo-habitat that contains
202  subtropical pelagic diatoms species that thrive in warm waters (Ren *et al.,* 2014), representing
203  the possible northward transport of warm to temperate waters into the GOA. The Shannon
204  Weaver Index (SWI) was calculated to quantify diatom diversity (Shannon & Weaver, 1949).

205  Diatom preservation is reconstructed to assess whether a water column silica rich or poor, with
206  longer or lower exposure of silica to degradation due to slower or more rapid sediment burial.
207  Following observations with light microscopy, three main states of valve preservation were
208  defined as: (1) good or no significant enlargement of the areolae or dissolution of the valve
209  margin; (2) moderate where valves show areolae enlargement, dissolution of the valve margin
210  and valve fragmentation; and (3) poor or strong dissolution of the valve margin and areolae
211  enlargement (Crosta *et al.*, 2012; Romero *et al.*, 2005, 2009, 2012, 2015, 2017). In addition,
212  two intermediate states of dissolution characterize valves whose state of preservation does not
213  fully fit the three above-mentioned categories: good/moderate (good preservation
214  predominates over moderate preservation) and moderate/good (moderate preservation
215  predominates over good preservation).

216  Biogenic silica was determined with a sequential leaching technique with 1M NaOH at 85°C
217  (Müller & Schneider, 1993) and normalized to the weight of the sample (wt%) and
218  accumulation rates of the sediment (Equation 3). The precision of the overall method based on
219  replicate analyses varies between ±0.2 and ±0.4%, depending on the material analyzed.

220  3.4 Biomarker analyses.

221  The lipid biomarker extraction followed the microwave assisted extraction method of
222  Kornilova & Rosell-Melé (2003), and detailed in Sánchez-Montes *et al.,* (2020). To obtain *n*-
223  alkanes, aromatics, ketone, and polar fractions, total lipid extracts were separated using silica
224  column chromatography through sequential elution with hexane (3mL), hexane:

225 dichloromethane (9:1; 1.5mL), dichloromethane (5.5 mL), and ethylacetate : hexane (20 : 80;
226 four columns) (Sánchez-Montes *et al.,* 2020). Each fraction was analysed by Gas
227 Chromatography Mass Spectrometry (GC-MS) for compound identification, and Flame
228 Ionization Detector (GC-FID) where biomarkers were separated using a 60m x 0.25 mm i.d.,
229 Restek RXi-5ms column (0.25 m 5% diphenyl-95% dimethyl polysiloxane coating). Lipid
230 quantification was achieved with reference to the following internal standards: 5α- cholestane
231 for *n*-alkanes, 2-nonadecanone for ketones, and 5α-androstan-3β-ol for polars (Equation 5),
232 normalised to the original extracted dry weight of sediment and then calculated as mass
233 accumulation rates (MAR), to take into account the influence of changing sedimentation rate
234 and sediment density on original biomarker concentrations (Equation 3).

235 $\quad\quad$ **Equation 5:** Mass biomarker $(\mu g) = (\frac{\text{Mass standard } (\mu g)}{[\text{Area standard}]})$ [area biomarker]

## 4 Results

237 During the Pliocene-early Pleistocene, biogenic silica export to Site U1417 exceeds TOC by
238 15 times (Figure 2A and B). TOC is overall 10 times more abundant than TN (Figure 2B). As
239 part of the TOC, the sum of long-chain ($C_{27}$, $C_{28}$, $C_{31}$), or terrigenous, *n*-alkanes is overall 3
240 times higher than that of short chain ($C_{15}$, $C_{17}$, $C_{21}$), or aquatic, *n*-alkanes (Figure 2D). Aquatic
241 *n*-alkane MAR are 2 times higher than alkenone MAR (from haptophyte algae), which, in turn,
242 are 3 times more abundant than brassicasterol (from diatoms and haptophyte) (Figure 2E). The
243 main changes across the PPT (3.2-2.4 Ma) are the overall decrease in biogenic silica MAR,
244 increase in TOC MAR, TN MAR, terrestrial and aquatic *n*-alkane MARs and the decrease and
245 later (2.6 Ma) increase in $\delta^{13}C$ and $\delta^{15}N$ (Figure 2). Maxima in *n*-alkanes, alkenones and
246 brassicasterol are observed during the early Pleistocene (2.4-1.7 Ma, Figure 2D and E).

247 Diatoms and silicoflagellate MAR are highest during the early part of the record (4.0-3.8 Ma,
248 Figure 3A), with coastal high productivity diatoms as the most abundant group at Site U1417
249 followed by benthic, coastal moderate productivity, pelagic warm and freshwater diatoms
250 (Figure 3, Table S2). Across 3.7 to 2.8 Ma, diatoms and silicoflagellate MAR decrease
251 progressively. Silicoflagellates disappear by 3.35 Ma, whereas diatoms almost disappear by
252 2.8 Ma (Figure 3A). The diatom assemblages recorded at Site U1417 switch from coastal high
253 productivity to dominantly pelagic high productivity groups across 3.7 to 2.8 Ma (Figure 3,
254 Table S2), particularly between 3.3 and 3.2 Ma. *Coscinodiscus marginatus*, the main species
255 contributing to the pelagic high productivity assemblage at Site U1417, is a minor component
256 of the diatom communities in the North Pacific across the Cenozoic, but it has been found
257 abundant in the subarctic Pacific and Bering Sea during the Late Pliocene (Shimada *et al.,*
258 2009).

259 The preservation of diatoms follows the same stepwise decline as the total diatom abundances,
260 where preservation is high during 4-3.7 Ma, decreases gradually across 3.7-3.2 Ma and
261 increases slightly between 3.19-2.8 Ma before diatoms almost completely disappear from the
262 record between 2.8-1.7 Ma (Figure 3B). Biogenic silica MAR decreases in response to the
263 decline in diatom MAR at 2.8 Ma (from an average of 0.39±0.057 to 0.31±0.016 g cm$^{-2}$ kyr$^{-1}$;
264 Figure 3A). The decrease in siliceous microfossils occurs during an increase of organic matter
265 concentrations (TOC and TN) across the PPT (Figure 4). The early Pleistocene increase in
266 organic matter content (Figure 4D) is also evident in the increasing biomarker concentrations
267 (Figure 4A, B and C). Signs of different production or selective organic matter degradation are
268 suggested by different patterns in the biomarkers i.e. peaks in alkenone often coincide with the
269 absence of sterols (Figure 4A and B).

## 5 Discussion

271 Across 4.0-1.7 Ma, the marine productivity export to Site U1417 is characterised by changes
272 in the relative contribution of siliceous microfossils and organic matter (Figure 4). These
273 changes culminate with an increase in organic matter export and almost complete
274 disappearance of siliceous remains across the PPT and early Pleistocene (Figure 4). A range of
275 factors could explain the siliceous/organic matter export changes, including (i) changes in
276 nutrient supply and phytoplankton production, (ii) water column stratification and carbon/silica
277 preservation, and/or (iii) the impact of sedimentation rate on phytoplankton burial efficiency
278 and preservation. Here we examine chronologically the forcings and responses behind the
279 siliceous and organic matter productivity export changes. According to these changes, the
280 record can be divided into three intervals: the early Pliocene (4.0-3.8 Ma), the late Pliocene
281 (3.7-2.82 Ma), and the PPT and early Pleistocene (2.8-1.66 Ma).

282 5.1 The early Pliocene (4.0-3.8 Ma): high biogenic silica export of high productivity coastal
283 habitats.

284 The maximum MAR of diatoms (up to $100*10^6$ valves $cm^{-2}$ $kyr^{-1}$, Figure 3A) and
285 silicoflagellates (up to $0.3*10^6$ valves $cm^{-2}$ $kyr^{-1}$, Figure 3A) suggests increased marine
286 productivity at Site U1417 during the early Pliocene. The high SWI indicates a highly diverse
287 diatom community (Figure 3B) at Site U1417, where diatoms originate from a range of
288 habitats: coastal high productivity, benthic, pelagic high productivity, coastal moderate,
289 pelagic warm and freshwater (from most to least abundant, Figure 3, Table S2). The biogenic
290 silica concentrations are also high, which accounts for the productivity, preservation and valve
291 sizes of a number of siliceous microorganisms such as diatoms, silicoflagellates and
292 radiolarians, the last two being less abundant at Site U1417 than diatoms.

293 The most prolific diatoms are *Chaetoceros* resting spores (up to $68*10^6$ valves $cm^{-2}$ $kyr^{-1}$,
294 Figure 3C, Table S2) which are abundant in high productive coastal waters in the GOA (e.g.,
295 Ren *et al.,* 2014). *Chaetoceros* dominate the diatom community of the GOA when iron is added
296 to the North Pacific (Tsuda *et al.,* 2003) and they develop resting spores after nutrient
297 consumption (Margalef, 1978). Therefore, the prolific coastal diatom productivity suggests
298 iron supply from the nearby continent and shelves to the neritic zone of the GOA (e.g., Ren *et
299 al.,* 2014, Lam & Bishop, 2008). The marine productivity species at Site U1417 suggest a
300 productivity gradient during this time less steep towards the coast compared to present (Figure
301 1), where the maximum productivity export of diatoms occurs.

302 The low contribution of pelagic diatoms and marine biomarkers (brassicasterol, alkenones and
303 aquatic *n*-alkane MAR) suggests a limited open-ocean productivity in the GOA (Figure 4A, B
304 and C). This causes a contrast between a highly productive coastal zone which supported
305 diatom productivity in coastal habitats to the detriment of pelagic diatom, coccolithophores
306 and other marine phytoplankton productivity (Herbert, 2001). The regime of abundant micro-
307 nutrients and low macro-nutrients known as LNHC characterises the modern coastal Alaska
308 (Weingartner, 2007). The source of micro-nutrients during the Pliocene could be from two
309 terrestrial sources: glacial flour and/or aeolian dust (Müller *et al.,* 2018; Romero *et al.,* 2022).
310 Iron-rich glacial flour is abundant in modern coastal Alaska estuaries e.g., the Copper River
311 (Crusius *et al.,* 2011) and the continental margin (Lam and Bishop, 2008). Wind transport is
312 an important mechanism today for transporting dust from Alaska hundreds of kilometres
313 beyond the shelf break to the GOA (Crusius *et al.,* 2011, Crusius *et al.,* 2017). However, high
314 pollen abundance at Site U1417 during the early Pliocene suggests higher riverine terrestrial
315 input from coastal Alaska to the GOA (Pisias *et al.,* 2001; Sanchez-Montes *et al.,* 2020). The
316 presence of freshwater diatoms contributing around 1% to the total diatom concentration in the
317 GOA is most likely attributed to Alaskan aeolian dust transport (Figure 4B) (e.g., Crusius *et
318 al*., 2011, Crusius *et al.,* 2017). Coastal diatoms have been previously interpreted as downslope

319  transport inputs to Site U1417 from the coastal area (Jaeger *et al.,* 2014). Another explanation
320  is the ocean fertilisation by dust nutrient delivery and increase in coastal diatom productivity.

321  The 30% contribution of benthic diatoms to the total diatom MAR at Site U1417, despite its
322  location at 4,218 m water depth (Jaeger *et al.,* 2014), points to the transport of shallow water
323  habitat assemblages towards the Surveyor Fan (McGee *et al.,* 2008). The early Pliocene
324  lithology at Site U1417 contains gravity flow deposits, while the tectonic history in the GOA
325  and coastal Alaska during the Pliocene (Enkelmann *et al.,* 2015) may result in slope instability
326  and distal transport of shallow species to Site U1417, which lies ~700 km from the coastline
327  (comparable to distances observed in turbidity current transports offshore West Africa, Talling
328  *et al.*, 2021). Relatively high terrestrial *n*-alkane MAR (Figure 4C) suggest enhanced flux of
329  terrestrial OM input and rapid burial during gravity flows, which may also account for the
330  peaks in TOC (e.g., Hage *et al.,* 2020). Plant fragments were also observed at Site U1417, and
331  attributed to both mature (Rea *et al.,* 1995; Gulick *et al.,* 2015) and fresh (Jaeger *et al.*, 2014)
332  origins (Sánchez-Montes *et al.,* 2020). High TN (Figure 4D) and $\delta^{15}N$ values of 3.7‰ (Figure
333  2C) suggest around 50% terrestrial origin of nitrogen at Site U1417 (Walinsky *et al.,* 2009). In
334  addition to the tectonic framework of the GOA, the presence of freshwater diatoms at Site
335  U1417 (Figure 4B) could support the importance of river transport and glacial development to
336  trigger slope instability and gravity flows (e.g., Pope *et al.,* 2018; Hage *et al.,* 2019).

337  The early Pliocene contains the highest concentration of benthic and freshwater diatoms
338  (average 15%) known to synthesize brassicasterol (e.g., Rampen *et al.,* 2010; Piepho *et al.,*
339  2011) found at U1417 (Table S2), yet brassicasterol concentrations are low during the early
340  Pliocene. Low brassicasterol concentrations could reflect organic matter degradation or less
341  favourable (nutrient) conditions for brassicasterol producers (Goad & Withers, 1982;
342  Kanazawa *et al.,* 1971; Lei *et al.*, 2012; Müller *et al.,* 2011; Volkman, 2006; Volkman, 1986).

343  The high diatom productivity (high diatom MAR) may have been supported by an abundant
344  ocean carbon pool with widely available $^{12}C$, as shown by low bulk $\delta^{13}C_{org}$ at this time (-24.7‰,
345  Figure 2C). A large carbon pool could suggest a very well mixed and oxygenated ocean. An
346  oxygenated water column would also favour silica preservation rather than organic matter
347  preservation, as observed in Site U1417 (Figure 4A and B, Figure 5B and C). The oxygenated
348  water column, perhaps aided by oxygen transport via turbidity currents, downwelling
349  movement of water masses and ocean mixing, could explain the low concentration of marine
350  biomarkers in the GOA during the early Pliocene (Figure 6). The low sedimentation rates
351  during the early Pliocene might also have favoured organic matter degradation at the sediment-
352  water interface due to longer exposure to oxidising conditions outside of the gravity flow events
353  (Figure 4A).

354  5.2 The late Pliocene (3.7-2.82 Ma): decrease in terrestrial and coastal biogenic silica and
355  increase in marine productivity.

356  The decrease in diatom and silicoflagellate MAR (Figure 3A) during the late Pliocene seems
357  to be caused by a decrease in flux and silica preservation (e.g. Thunell *et al.,* 1994; preservation
358  value, Figure 3B) and is accompanied by an increase in the number of pelagic diatom species
359  (Figure 3D). The main contributor to the total diatom MAR thus shifts from high productivity
360  coastal species during the early Pliocene (average of 54%) to a high productivity pelagic
361  environment during most of the late Pliocene (average of 56%; Figures 3C and D). These
362  ecological changes are accompanied by a higher diatom diversity during the late Pliocene than
363  during the early Pliocene (Figure 3B), which could partially explain a small increase in
364  biogenic silica preservation from the previous period (Figure 2A).

365　The disappearance of silicoflagellates from the record at 3.35 Ma (Figure 3A) occurs with an
366　increase in organic matter inputs to Site U1417. The progressive increase in productivity
367　indicators from coccolithophores (e.g., alkenones; Figure 4B) and other phytoplankton (aquatic
368　*n*-alkanes, Figure 4C) alongside increasing TOC and TN (Figure 4D) suggests better organic
369　matter preservation and/or increasing export production from marine sources. Terrigenous *n*-
370　alkanes decrease during most of the late Pliocene (Figure 4C) suggesting a reduction in land
371　vegetation and/or a reduced riverine/aerial terrestrial plant transport to Site U1417, also
372　suggested by an overall decrease in freshwater diatoms (Figure 4B). Progressively increasing
373　$\delta^{13}$C but decreasing $\delta^{15}$N across the late Pliocene suggests a limited carbon but abundant
374　bioavailable nitrogen pool for phytoplankton consumption (Figure 2C). A reduced ocean
375　mixing/more stratified water column, caused by slow ocean circulation or reduced gravity flow
376　movement, would limit the atmosphere-ocean $^{12}$C exchange and increase bacterial nitrogen
377　fixation (Galbraith *et al.,* 2004).

378　The continuous presence of benthic diatoms suggests that downslope transport towards Site
379　U1417 still occurred during the late Pliocene but was reduced. The decrease in river transport
380　could reflect an increasingly glaciated landscape, as suggested in Sánchez-Montes *et al.* (2020),
381　which is supported by higher sedimentation rates (Figure 5D; Gulick *et al.,* 2015). Reduced
382　downwelling is suggested by decreased silica preservation and increased organic matter
383　preservation. Further, the LNHC region in the GOA reduced in extent due to a higher
384　macronutrient availability and allowed the expansion of marine pelagic communities across a
385　range of producers (including diatoms and coccolithophores, Figure 3D and 4B) and increased
386　the overall ocean diversity (Figure 3B). In addition, the less mixed water column would have
387　favoured bacterial nitrogen fixation (Galbraith *et al.,* 2004), phytoplankton nitrogen
388　consumption and phytoplankton nitrogen burial (Figure 4D).

389　As the glaciation progressed during the late Pliocene, there is evidence of tectonic uplift and
390　glaciations causing changes in the Alaskan landscape such as a shift in the Yukon River flow,
391　from originally southward direction to the GOA to flow westward to the Bering Sea (Duk-
392　Rodkin *et al.,* 2004), which would have reduced riverine terrestrial and freshwater input to the
393　GOA. Similarly, reversal of the Bering Strait throughflow from southward to northward at 3.6
394　Ma (Horikawa *et al.,* 2015) away from the North Pacific to the Arctic Ocean, may also have
395　impacted the ocean circulation in the GOA. The resulting enhanced organic matter MAR from
396　reduced river runoff and decrease in strength of ocean currents in the GOA could reflect
397　improved preservation resulting from a more stratified water column.

398　The MPWP (3.33-3.19 Ma) is noted separately here as it has several specific characteristics
399　which are different from the rest of the Pliocene at Site U1417. Although there is a sharp
400　reduction in diatom MAR (3.25-3.19 Ma; Figure 4A) elevated marine export productivity is
401　indicated by high abundances of pelagic diatom species (with an average of 88%, Figure 3D)
402　accompanied by peaks in brassicasterol (Figure 4A), alkenones (Figure 4B) and aquatic *n*-
403　alkane (Figure 4C) MAR, alongside peaks in Ba/Al (330-350 ppm % $^{-1}$) and $CaCO_3$ (<2 %) at
404　Site U1417 (Zindorf *et al*., 2019; Jaeger *et al.,* 2014). The higher susceptibility of brassicasterol
405　than alkenones to degradation (Gaskell *et al.,* 1974; Wakeham *et al.,* 2002) suggest a combined
406　favouring of water chemistry and nutrient regime for brassicasterol producers (diatoms) to the
407　detriment of alkenone producers (haptophyte). The reduced diatom diversity and shift to
408　increasingly open ocean productivity conditions, dominated by pelagic high productivity
409　environments, is consistent with the reduction of diatom biodiversity in other marine habitats
410　(Figure 5B) (Nakov *et al.,* 2019).

411　The driver(s) for the enhanced MPWP marine production at Site U1417 could reflect enhanced
412　nutrient supply to the centre of the Alaskan gyre as productivity gradients relax during warmer

intervals (Figure 1) and/or improved preservation of the productivity proxies. There is a sharp reduction in benthic and coastal high productivity diatoms during the MPWP since the marine isotope stage M2, suggesting that gravity flows decreased, which may have been aided by a decrease in riverine inputs due to the expansion of mountain glaciation in Alaska (Horikawa *et al.,* 2015; Sánchez-Montes *et al.,* 2020). Peaks in terrestrial *n*-alkane MAR show that erosion and transport of terrestrial material to the site was still occurring, potentially by wind and/or glaciers if riverine inputs were reduced (e.g., Müller *et al.,* 2018; Sánchez-Montes *et al.,* 2020). These terrestrial inputs would likely still have provided a source of terrestrial iron. The general increase in ocean productivity (Figure 5B) during colder periods of the MPWP suggests increased atmosphere and ocean circulation and increased deep nutrient availability to the photic zone of the GOA under a HNLC region. Stratification during warmer periods of the MPWP would have been achieved by ice melting and increased ocean heat absorbance (e.g., Behera *et al.*, 2021) while the MPWP poleward shift of the westerly winds might have been able to occasionally break the stratification in the GOA (Abell *et al.,* 2021).

The overall sluggish circulation during the late Pliocene may suggest an ocean circulation reorganization in the GOA after the northward shift of the Yukon River outlet and Bering Strait throughflow. An interesting increase in pelagic warm water productivity (up to 45% of diatoms) might shed some light on the origin of the first $C_{37:4}$ peak above 5% in the GOA at 3.0 Ma, interpreted as the first evidence of glacier tidewater freshwater runoff in the GOA since 4.0 Ma (Sánchez-Montes *et al.,* 2020). This could indicate that ice (i.e. tidewater glaciers) might have developed in the coastal GOA during the MPWP, the terminus of which might then have been melted by the northward advection of warm Pacific waters, such as the NPC (Figure 1). The injection of warm waters from lower latitude North Pacific to the GOA (shown by pelagic warm diatoms) and an increase in coastal moderate productivity diatoms seem to anticipate blooms in the gyre diatom communities (peaks in pelagic high productivity diatoms) characterising the transitional diatom communities during the late Pliocene. The new oceanography and reduction of freshwater input to the GOA allowed the Alaskan gyre to bring warm NPC waters to Site U1417. It might be that the new ocean configuration in the GOA with higher influence from lower latitudes during the late Pliocene allowed the rapid expansion of the CIS (Sánchez-Montes *et al.,* 2020).

5.3 The late Pliocene - early Pleistocene (2.8-1.66 Ma): increase in organic matter export.

The change from higher siliceous to higher organic matter productivity export, first observed in our record during the MPWP, becomes a permanent characteristic during the PPT and early Pleistocene (2.8-1.66 Ma; Figures 4A and B). The dominant pelagic contribution from diatoms to the productivity export since 2.8 Ma suggests that the alkenone MAR indicates total productivity export (Raja & Rosell-Melé, 2021) where the productivity was higher in central GOA and the productivity gradient shifted towards the coast (Figure 1). From 2.8 Ma, diatoms almost completely disappear from the record and TOC, TN and biomarkers increase more rapidly (Figure 4). Concentrations in terrestrial *n*-alkanes also increase but also become more variable, suggesting a mixture of transport mechanisms at play e.g., wind and glacial runoff (Figure 4D). The synchronous response of increasing terrigenous and aquatic *n*-alkanes seems to reflect ocean fertilisation through wind and/or glacial runoff-derived nutrients (Figure 4C, Figure 5 C and D).

We propose that the increase in pelagic productivity from 2.8 Ma occurred under a strong Alaska gyre fuelled by an Aleutian Low (AL) centred in the GOA (Sancetta & Silvetri, 1986) and highly functioning ocean-ice-climate linkages (Sánchez-Montes *et al.,* 2020) which favoured ocean fertilisation (Figure 6). Frequent glacial meltwater influence in the GOA is supported by peaks in $C_{37:4}$ above 5% after 2.8 Ma (Sánchez-Montes *et al.*, 2020, Figure 5C),

461    where sea-ice (Wang *et al.,* 2021) at Site U1417's climatic setting likely played a minor role.
462    A stratified and warmer water column (Figure 5A and C) could suggest a decrease in oxygen
463    availability in the surface ocean and a shallower remineralisation depth that favoured the
464    carbon pump (Crichton *et al.,* 2021). Warm intervals of the GOA have previously been linked
465    to a decrease in dissolved oxygen (Galbraith *et al.,* 2004; Barron *et al.,* 2009; Zindorf *et al.,*
466    2020). Since the late Pliocene until 2.4 Ma, the $\delta^{13}$C and $\delta^{15}$N display a variable but an overall
467    decreasing trend, suggesting a progressively larger pool of carbon and bioavailable nitrogen
468    feeding the marine phytoplankton. The increase in organic nitrogen during 2.8-2.4 Ma suggests
469    a slow ocean circulation and an overall stratified water column (Galbraith *et al.,* 2004), storing
470    nutrients in the deeper ocean, where nitrogen could become bioavailable by increased nitrogen
471    fixation and would become available to the surface with episodes of ocean mixing. During the
472    early Pleistocene (2.4-1.66 Ma) the $\delta^{13}$C remains low, however the $\delta^{15}$N increases suggesting
473    an increase in inorganic nitrogen supply (Figure 3C).

474    The higher alkenone and brassicasterol (haptophyte and diatoms) export suggests that the GOA
475    iron abundance decreased region during the late Pliocene-early Pleistocene similarly to during
476    the MPWP and at modern times (Martin and Fitzwater, 1988; Martin *et al.*, 1991; Hinckley *et*
477    *al.*, 2009). The marine productivity was controlled by the availability of nutrients accumulated
478    in the deep GOA, made available when increased wind speeds increased ocean mixing,
479    interrupting an otherwise highly stratified water column configuration (peaks in alkenones and
480    brassicasterol, Figure 4A and B; Abell *et al.,* 2021; Sánchez-Montes *et al.*, 2020). The highest
481    TOC and TN of the record are found between 2.4 and 1.66 Ma suggesting the highest carbon
482    and nitrogen deep ocean storage. However, TOC and TN show a slowly decreasing trend
483    which, together with similar $\delta^{13}$C and an increase in $\delta^{15}$N from the previous interval (2.8-2.4
484    Ma), suggests a shift towards reducing organic carbon export to the deep sea, perhaps reflecting
485    enhanced respiration in the water column and return of carbon to the atmosphere under an
486    intensified ocean circulation (Galbraith *et al.*, 2004). A better ventilated ocean is consistent
487    with the frequent peaks in terrestrial *n*-alkanes attributed previously to strong winds, which
488    could have promoted oxygenated conditions in the GOA, consistent with our observed decrease
489    in brassicasterol preservation and increased diatom concentrations (although still very low,
490    0.04-0.4 Million valves cm$^{-2}$ kyr$^{-1}$) (Figure 4). The increase of diatoms (2.0-1.66 Ma) supports
491    the aeolian supply of terrestrial nutrients, possibly aided by glacial meltwater input. Upwelling
492    centred in the GOA and ocean fertilization is a characteristic of the northeast Pacific at present
493    under the influence of the AL atmospheric circulation and HNLC configuration.

494    During 2.4-2.0 Ma, the increase in alkenone MAR (Figure 4A and B) and the fragmentary
495    brassicasterol record suggest a less stratified ocean column and increased upwelling conditions
496    in the HNLC region. Intensified winds during 2.4-1.66 Ma (deduced from high terrestrial *n*-
497    alkane concentrations) under the influence of the AL and increased deep ocean mixing due to
498    increased gyre circulation might have been responsible for the increases in terrestrial input and
499    deep nutrient availability in the photic zone, respectively, corresponding to a HNLC region.
500    The increase in nutrient availability resulted in a higher marine productivity export and high
501    carbon and nitrogen deep storage (high TN, TOC; Figure 5E) which suggests a still strongly
502    reductive ocean interior.

503    5.4 Implications for ocean circulation and CO$_2$ storage in the GOA during the CIS
504    development.

505    We have outlined several scenarios of changing Pliocene and early Pleistocene productivity in
506    the GOA, as well as changes in likely nutrient sources. The biogeochemical changes in the
507    water column described at Site U1417 follow an eccentricity-driven ~400 kyr cyclicity (Figure
508    3). Although the patterns are complex, we note that low eccentricity periods can be linked to

509 surface ocean cooling and changes in the CIS extent (Figure 5). We suggest here that this in
510 turn resulted in impacts on nutrients and productivity offshore linked to changes in the Alaskan
511 and the Aleutian Low (Sancetta & Silvestri, 1986; Barron, 1998). We propose that eccentricity
512 minima and cooler periods on land triggered an increased glaciation and changed the regional
513 oceanography of the GOA via internal feedback mechanisms. For example, the disappearance
514 of silicoflagellates (3.48 Ma), the reduced diatom productivity export (M2 and KM2) and the
515 disappearance of diatoms (2.8 Ma) all mark the Pliocene ~400kyr eccentricity cycles of silica
516 dissolution under increased ocean reductive conditions linked to a shift towards increased gyre
517 circulation.

518 The 100 kyr cycles of lower amplitude eccentricity changes linked to a slightly more active
519 gyre circulation are also reflected in relatively cool periods such as the Gi4 at 3.65 Ma and Gi2
520 at 3.60 Ma. Stage Gi4 impacted productivity export by decreasing the terrestrial freshwater
521 diatom input to Site U1417, the latter by dissolving the silica momentarily from the record.
522 Peaks in alkenone MAR at Site U1417 mark the 400 kyr and some 100 kyr low eccentricity
523 events and could be attributable to a higher biological pump during cooler climate (Boscolo-
524 Galazzo *et al.,* 2021; Crichton *et al.,* 2021; Figure 4B). These low eccentricity conditions
525 intensified overall during the CIS expansion at 2.8 Ma (Figure 5), where the Alaskan gyre
526 became more active driving pelagic productivity at the centre of the GOA. Decrease in diatom
527 and increases in pelagic high productivity at the centre of the Alaskan gyre suggests a steep
528 productivity gradient shifted towards the coastal region (Figures 4 and 5) (Barron*,* 1998).
529 Productivity peaks in the subarctic Pacific have been associated with lower dissolved oxygen
530 under warmer climate (Barron *et al.,* 2009; Knudson *et al.,* 2021), which suggests a more
531 reductive ocean during the PPT and an increase in carbon burial efficiency (Lopes *et al.,* 2015).
532 Lower productivity during warmer SSTs, with a stratified ocean and increased atmospheric
533 oxygen, has also been suggested due to a higher carbon remineralisation in the water column
534 and lower C pump (Boscolo-Galazzo *et al.,* 2021; Fakhraee *et al.,* 2020; Komar & Zeebe, 2021;
535 Crichton *et al*., 2021). However, in the northeast Pacific, ecosystem and sea-floor controls have
536 been identified as playing a bigger role than SST to increase carbon export despite lower
537 productivity (Lopes *et al.,* 2015). In addition, under a warmer climate and more stratified
538 ocean, productivity export has been suggested to increase due to an increase in carbon
539 remineralisation in the upper ocean resulting in increase in productivity, whereas the carbon
540 pump remains largely similar before and after warming (Crichton *et al.,* 2021). SSTs increase
541 ~1°C at Site U1417 during the early Pleistocene in comparison with the late Pliocene (Sánchez-
542 Montes *et al*., 2020). An SST increase of 0.6 °C is estimated to reduce by 5% the particulate
543 organic carbon at a 1 km water column depth (Crichton *et al.,* 2021). Carbon remineralisation
544 at 4 km deep (Site U1417) is therefore likely to have contributed minimally to decrease C
545 export across the Plio-Pleistocene, where other sites in the northeast Pacific register lower SSTs
546 (Sánchez-Montes *et al*., 2020). As a result, we do not think that changes in organic matter
547 remineralisation in response to changing ocean temperatures can account for the shift in MAR
548 we identify here, leaving a change in export production as the most likely driver of the changes
549 we observe. During the CIS retreat at 1.9 Ma, offshore productivity is high as well as the
550 transport of coastal productivity diatoms returns to Site U1417 suggesting an increase in iron
551 delivered to the GOA (Costa *et al.,* 2017) and a return to slightly more oxygenated conditions.

552 Site U1417 sits in the Surveyor Fan while ODP 887 sits in the Aleutian Abyssal Plain (Rea &
553 Snoeckx, 1995). While we note an apparent higher terrigenous input at ODP 887 than U1417
554 across the Pliocene and early Pleistocene (Figure 7), these records need to be considered to
555 reflect different environmental proxies (coarse and fine mineral clasts vs. long-chain n-alkanes,
556 respectively) and settings. Sedimentation rates are higher at Site U1417 than ODP 887 across
557 the Pliocene and early Pleistocene (Jaeger *et al.,* 2014; Rea & Snoeckx, 1995) suggesting

558  higher terrigenous inputs to Site U1417 than ODP 887, which is explained by proximity to the
559  CIS (ODP 887 is located 200 km southwest of U1417, further away from the CIS; Figure 7).
560  Site U1417 recorded similar biogenic silica MAR to ODP 887 (3,634-meter water depth,
561  Figure 7). Compared to other sites of the North and equatorial Pacific, ODP 887 and Site U1417
562  contain the lowest biogenic silica and alkenone MAR during the Pliocene-early Pleistocene
563  (Figure 7). This could suggest a similar biogenic silica preservation across the east subarctic
564  Pacific due to more oxygenated/reduced water column (Galbraith *et al.,* 2004), where ODP
565  887, closer to the centre of the AL suffered larger variations in silica preservation than Site
566  U1417 which is located under the AC (Figure 7). Comparing the subpolar gyre, which expands
567  across Site U1417, ODP 887 and ODP 882, there is an order of magnitude higher biogenic
568  silica MAR at ODP 882, under the influence of the Kamchatka Current in the west subarctic
569  Pacific (3,244 m water depth) than in the GOA (Figure 7). The highest alkenone MAR are
570  recorded at Site 1012, under the influence of the California Current (1,772 m water depth,
571  Figure 7), followed by ODP 846 under the Peru Current and close to the Equatorial
572  Undercurrent (3,307 water depth, Figure 7). According to these patterns, the sites located in
573  shallower water depths exhibited the highest productivity MAR, which suggests better
574  preservation but could also suggest that shallower water columns were more easily mixed or
575  had greater terrestrial nutrient supply to trigger productivity blooms.

576  However, as noted for Site U1417, the PPT development of the CIS and the NHG more
577  generally affected the preservation of siliceous and organic matter remains in the whole North
578  Pacific, where biogenic silica decreases and organic matter increases (Figure 7). In addition,
579  terrestrial inputs during the PPT increase, suggesting ocean fertilisation and an increase in
580  marine productivity in the northeast and possibly the equatorial Pacific (Figure 7). In particular
581  across 2.4-2.0 Ma, ocean fertilisation and productivity at the North Pacific Site U1417 and
582  ODP 1012 are maximum during the increase in gyre circulation (e.g. Barron *et al.,* 2002) and
583  increase in AL and North Pacific High systems, which suggest an increase in the westerly wind
584  strength (Abell *et al.,* 2021). The east equatorial Pacific, however, shows a decrease in
585  coccolithophore productivity probably explained by weaker trade winds at ODP 846 and
586  disruptions in the Pacific Cold Tongue (Liu *et al.,* 2019). From all regions represented in Figure
587  7, ODP 846 is the only region that cooled across the PPT (Sánchez-Montes *et al*., 2020),
588  supporting weaker trade winds and a rapid switch from La Niña to El Niño-like conditions.
589  The same northeast Pacific productivity and terrigenous input pattern observed for 2.4-2.0 Ma
590  also appears during the MPWP, when a weaker east equatorial Pacific upwelling system
591  suggests an expansion of the equatorial warm pool (Liu *et al.,* 2019). The expansion of the
592  equatorial warm pool also suggests a nutrient leakage of deep ocean nutrients (macronutrients)
593  to northern latitudes and a drier Asian continent to increase in dust (micronutrients) from the
594  Loess Plateau to the North Pacific (Abell *et al.,* 2021), driving the highest sustained
595  coccolithophore productivity between 2.4 and 2.0 Ma and the shift to open ocean productivity
596  during the MPWP and HNLC conditions. The nutrient leakage from the equatorial to the North
597  Pacific seems to have also played a role in the biogeochemistry changes observed at Site U1417
598  discussed above. Furthermore, these mechanisms aid a detachment from the aeolian and the
599  riverine/glacial terrigenous *n*-alkane signal. The highest peaks in terrigenous *n*-alkanes at Site
600  U1417 seem to be driven by an increase of terrigenous inputs from the Loess Plateau under a
601  stronger atmospheric and ocean circulation (Abell *et al.,* 2021), whereas the background
602  (smaller) peaks seem to correlate with increase in riverine/glacial terrigenous inputs from the
603  GOA (Figure 7D). Source studies of terrestrial input to Site U1417 during the PPT and early
604  Pleistocene suggest similar to modern coastal detrital provenance of Alaskan coast and Asia
605  (Rea *et al.,* 1995, Horikawa *et al.,* 2015) of the inorganic nitrogen and iron input to Site U1417
606  (Figure S1). The erosion of lithologies at lower altitudes as the glaciation progresses (Figure

607  S1, Perry *et al.*, 2009; Chapman *et al.,* 2012) is consistent with more recent source
608  interpretations in the GOA (Huber & Bahlburg, 2021).

609  In addition, the change in heat supply from the equator to the North Pacific due to
610  oceanographic changes might have resulted in the CIS glaciation attempt during the M2 (De
611  Schepper *et al.,* 2013) and CIS build up across the 2.4-2.0 Ma (Site U1417 highest
612  sedimentation rates, Figure 5D). The Kuroshio Extension characteristic microfossil tropical
613  species (Lam *& Leckie, 2020) and its increase at Site U1417 during stronger North Pacific
614  gyre circulation (Gallagher *et al.,* 2015) suggest the Kuroshio Extension influence in the GOA
615  since the late Pliocene (Gallagher *et al.,* 2015). The expanded storm track which characterises
616  modern El Niño (Joh *et al.,* 2021), in addition to a the permanent negative PDO-like climate in
617  the North Pacific across the Pliocene-early Pleistocene (Sánchez-Montes *et al*., 2020) and
618  mountain building (Enkelmann *et al.,* 2015) would increase ice accumulation on land under
619  lower atmospheric $CO_2$ concentrations (Figure 5A).

620  The eccentricity and biogeochemical changes observed in the GOA are observable in the North
621  Pacific, at least at the 400kyr cycles with some other cycles that are marked by eccentricity
622  minima at 3.8, 3.3, 3.2, 2.8, 2.4 and 2.0 Ma, where the subpolar gyre has been suggested to be
623  the driver of changes in the subtropical Pacific gyre (Sancetta & Silvestri, 1986). Despite higher
624  biogenic silica concentrations than Site U1417 before the PPT, ODP 882 and ODP 887
625  biogenic silica MAR decrease to comparable concentrations than Site U1417 after the PPT
626  resulting in an average homogeneous biogenic silica MAR of 0.4 g $cm^{-2}$ $kyr^{-1}$ across east and
627  west subarctic Pacific (Figure 7). The southward component of the Bering Sea (Horikawa *et
628  al.,* 2015) and the Yukon River flow during the early Pliocene (Duk-Rodkin *et al.,* 2004),
629  together with the productivity characteristics of the subarctic Pacific suggests that the early
630  Pliocene circulation in the North Pacific was different compared to modern, probably caused
631  by a different topography due to ongoing tectonic changes in coastal Alaska (Enkelmann *et al.,*
632  2015). However, during the PPT, the west subarctic Pacific and the Alaska gyre unified under
633  a HNLC region during the ocean reorganization across the late Pliocene and water column
634  stratification during iCIS. This suggests a closer cycling of ocean current between east and
635  west Pacific, with the Alaska Stream traveling westward in a subpolar gyre similar to present.
636  We further suggest that the new ocean configuration of strong Alaska Gyre and increased ACC
637  transport from the GOA through the Bering Sea towards the Arctic (Horikawa *et al.,* 2015)
638  may have contributed to freshening in the Arctic Ocean and sea-ice formation (Matthiessen *et
639  al.,* 2009).

640  Unlike the rest of the Pacific sites in Figure 7, the development of the subarctic Pacific HNLC
641  is a key region because increases in phytoplankton productivity and preservation associated
642  with the development of the CIS and water column stratification could impact the C budget via
643  atmospheric $CO_2$ drawdown. This is especially important considering that before the iCIS and
644  ocean stratification, the subarctic Pacific's effective respiration of organic matter would have
645  contributed to maintaining the high Pliocene $CO_2$ concentrations via ocean carbon degassing
646  (Figure 6). The subarctic Pacific HNLC region is subject to availability of micronutrients to
647  the photic zone (Crichton *et al.,* 2021) and therefore, the GOA closer to the CIS (in particular
648  Site U1417, which registers sedimentation rates four times higher than ODP 887, Jaeger *et al*.,
649  2014; Rea & Snoeckx, 1993) plays a key role in C fixation and burial. Considering the GOA
650  defined as the area contained within a line across the Kodiak Island and the Dixon Entrance
651  (USGS, 1981), the Surveyor Fan extends across two thirds of the GOA, the other one third is
652  occupied by the Baranoff Fan and ODP887, in the Aleutian Abyssal Plain, is excluded (Rea &
653  Snoeckx, 1993). The Surveyor and Baranoff Fans are similar in area and volume and share a
654  similar climatic and tectonic history, where they transitioned from riverine towards higher

655    glacial inputs through the Pleistocene, however the sediment provenance of the Baranoff Fan
656    in the Coast Mountains (Walton *et al.,* 2014) is different to the Surveyor Fan from the St. Elias
657    Mountains (Enkelmann *et al.*, 2014) and there is a lack of understanding of the area to date.
658    Based on the Surveyor Fan alone and assuming similar sedimentation rates and marine
659    productivity responses to the climate changes across the fan, increases in TOC MAR at Site
660    U1417 across the PPT results to an estimated 404 ±23 Pg carbon export increase in the
661    Surveyor Fan during the iCIS and early Pleistocene in comparison to the rest of the Pliocene.
662    The increase in organic carbon burial of the order of 186 ±20% in the Surveyor Fan occurred
663    during a period of 13 ±2% decrease in the global atmospheric $CO_2$ across the iCIS and early
664    Pleistocene (de la Vega *et al.*, 2020). This might suggest that despite the GOA is an small area,
665    the increase in the sediment rates and organic matter burial across the early Pleistocene could
666    have contributed to the global atmospheric $CO_2$ reduction. However, these numbers are
667    indicative only, and more research is needed to quantify the maximum and minimum extent of
668    carbon burial more accurately during the Plio-Pleistocene transition. Both elevated
669    productivity and better organic matter preservation could have been important for increasing
670    deep ocean and sediment storage of organic matter, and potentially drawing down atmospheric
671    $CO_2$ and cooling the climate (e.g., Burdige, 2007) under short (orbital) time scales (e.g., during
672    low eccentricity intervals in the MPWP; de la Vega *et al.,* 2020; Figure 5B), and longer time
673    scales (e.g., across the PPT). In addition, high marine diversity during the late Pliocene might
674    have slowly contributed to atmospheric $CO_2$ drawdown as suggested for the present day
675    (Palevsky *et al.,* 2013). Globally, the atmospheric $CO_2$ decreased about 100 ppm during the
676    PPT (Figure 5B), where 40% of the modern decadal atmospheric $CO_2$ variability has been
677    attributed to ocean forcing (DeVries *et al.,* 2019). Similarly as what we find in the GOA during
678    the PPT, carbon sinking at modern is accelerating in the Pacific (Carter *et al.,* 2019). Further
679    work is needed to estimate the GOA's contribution to global atmospheric $CO_2$ decrease during
680    the Pliocene and Pleistocene.

681    **6. Conclusions**

682    The Pliocene and early Pleistocene productivity at Site U1417 is characterised by a decrease
683    in siliceous microfossil export from coastal habitats and an increase in pelagic organic matter
684    productivity. We attribute this change to a biogeochemical shift from (i) oxygenated, high
685    micro-nutrient availability but low nitrogen bioavailability (low nutrient high chlorophyll,
686    LNHC region), to (ii) reductive deep Gulf of Alaska (GOA), with restricted macro and micro-
687    nutrients but high nitrogen bioavailability (high-nutrient-low-chlorophyll, HNLC region),
688    during the Plio-Pleistocene transition (PPT). We conclude that both tectonic uplift in the St.
689    Elias mountains since the Pliocene during short-lived low eccentricity cycles increased the
690    Cordilleran Ice Sheet glaciation and altered atmospheric and ocean circulation patterns, ocean
691    biogeochemistry, and marine productivity. The stronger eccentricity cycles (~400 kyr) marked
692    glacial events, with associated peaks in marine productivity export which could have drawn
693    down $CO_2$ from the atmosphere e.g., the KM2 at 3.2 Ma, at 2.8 Ma, 2.4 Ma and 2.0 Ma. In
694    contrast, during the shorter (100 kyr) higher eccentricity period glacials, climate feedback
695    mechanisms of increased glaciation on land, decrease riverine and terrestrial nutrient inputs to
696    the GOA derived in enhanced HNLC conditions and increased reductive conditions in the
697    GOA. Over longer time scales (PPT) the GOA is potentially an important region due to the
698    variability and, crucially, the increase in ocean fertilisation taking place. Changes in bottom
699    water conditions, in particular trends to more reductive conditions can potentially help to
700    account for increasing glaciation in Alaska, potentially having an impact on decreasing
701    atmospheric $CO_2$ concentrations and contributing to cooling the climate.

**Open Research**

The new datasets in this article are available at Pangaea (Sánchez-Montes *et al.* 2021).

**References**

Abell, J.T., Winckler, G., Anderson, R.F. & Herbert, T. D. (2021). Poleward and weakened westerlies during Pliocene warmth. *Nature* 589, 70–75. https://doi.org/10.1038/s41586-020-03062-1.

Addison, J., A., Finney, B. P., Dean, W. E., Davies, M. H., Mix, A. C., Stoner, J. S. & Jaeger, J. M. (2012). Productivity and sedimentary d$^{15}$N variability for the last 17,000 years along the northern Gulf of Alaska continental slope. *Paleoceanography*, Vol 27, PA 1206.

Andreev, A. A., Tarasov, P. E., Wennrich, V., Raschke, E., Herzschuh, U., Nowaczyk, N. R., Brigham-Grette, J., & Melles, M. (2014). Late Pliocene and Early Pleistocene vegetation history of northeastern Russian Arctic inferred from the Lake El'gygytgyn pollen record. *Clim. Past*, 10, 1017–1039. https://doi.org/10.5194/cp-10-1017-2014.

Ausín, B., Bruni, E., Haghipour, N., Welte, C.Bernasconi, S. M. & Eglinton, T. I. (2021). Controls on the abundance, provenance and age of organic carbon buried in continental margin sediments. *Earth and Planetary Science Letters*, 558, 116759, ISSN 0012-821X. https://doi.org/10.1016/j.epsl.2021.116759.

Ausín, B., Magill, C., Haghipour, N., Fernández, Á., Wacker, L., Hodell, D. *et al*., (2019). (In)coherent multiproxy signals in marine sediments: Implications for high-resolution paleoclimate reconstruction. *Earth and Planetary Science Letters,* 515, 38-46, ISSN 0012-821X. https://doi.org/10.1016/j.epsl.2019.03.003.

Barron, J. A. (1998). Late Neogene changes in diatom sedimentation in the North Pacific. *Journal of Asian Earth Sciences*, 16(1) 85-95. https://doi.org/10.1016/S0743-9547(97)00046-9.

Barron, J. A., Bukry, D., Dean, W.E., Addison, J. A. & Finney, B. (2009). Paleoceanography of the Gulf of Alaska during the past 15,000 years: Results from diatoms, silicoflagellates, and geochemistry. *Marine Micropaleontology*, vol. 72, issue 3-4, pp. 176-195.

Barron, J. A., Lyle, M. & Koizumi, I. (2002). Late Miocene and early Pliocene biosiliceous sedimentation along the California Margin. Revista Mexicana de Ciencias Geológicas, vol. 19, 003, 161-169.

Behera, P., Tiwari, M., & Knies, J. (2021). Enhanced Arctic stratification in a warming scenario: Evidence from the Mid Pliocene warm period. *Paleoceanography and Paleoclimatology*, 36.

747  Bender, A.M., Lease, R.O., Corbett, L.B., Bierman, P. R., Caffee, M. W. & Rittenour, T. M.
748  (2020). Late Cenozoic climate change paces landscape adjustments to Yukon River capture.
749  *Nature Geosciences* 13, 571–575. https://doi.org/10.1038/s41561-020-0611-4.

750  Berger, A. & Loutre, M-F. (1999). Parameters of the Earth's orbit for the last 5 Million years
751  in 1 kyr resolution, *PANGAEA*. https://doi.org/10.1594/PANGAEA.56040.

752  Blaauw, M. & Christen J.A. (2011). Flexible paleoclimate age-depth models using an
753  autoregressive gamma process. Bayesian Anal 6(3):457–474.

754  Bourbonniere, R.A. & Meyers, P.A. (1996). Sedimentary geolipid records of historical changes
755  in the watersheds and productivities of Lakes Ontario and Erie, *Limnology and Oceanography*
756  41, 352–359.

757  Boyer, T.P., Antonov, J. I., Baranova, O. K., Coleman, C., Garcia, H. E. & Grodsky, A., *et al*.
758  (2013). World Ocean Database 2013, *NOAA Atlas NESDIS 72*, S. Levitus, Ed., A. Mishonov,
759  Technical Ed.; Silver Spring, MD, 209 pp., http://doi.org/10.7289/V5NZ85MT

760  Burdige, D. J. (2005). Burial of terrestrial organic matter in marine sediments: A re-
761  assessment. *Global          Biogeochemical          Cycles*, 19,          GB4011.
762  https://doi.org/10.1029/2004GB002368.

763  Burdige, D. J. (2007). Preservation of organic matter in marine sediments: Controls,
764  mechanisms, and an imbalance in sediment organic carbon budgets*? Chemical*
765  *Reviews*, 107(2), 467–485. https://doi.org/10.1021/cr050347q.

766  Carter, B. R., Feely, R. A.,Wanninkhof, R., Kouketsu, S.,Sonnerup, R. E., Pardo, P. C., *et al*.
767  (2019). Pacific anthropogenic carbon between 1991 and 2017. GlobalBiogeochemical
768  Cycles,33, 597–617. https://doi.org/10.1029/2018GB006154.

769  Chapman, J.B., Pavlis, T.L., Bruhn, R.L., Worthington, L.L., Gulick, S.P.S., & Berger, A.L.
770  (2012). Structural relationships in the eastern syntaxis of the St. Elias orogen, Alaska.
771  *Geosphere,* 8, 105–126. https://doi.org/10.1130/GES00677.1.

772  Childress, L. B. (2016). The Active Margin Carbon Cycle: Influences of Climate and Tectonics
773  in Variable Spatial and Temporal Records, PhD thesis. *Northwestern University*, Evanson,
774  Illinois.

775  Cortese, G., Gersonde, R., Hillenbrand, C.-D. & Kuhn, G. (2004). Opal sedimentation shifts in
776  the World Ocean over the last 15 Myr. *Earth Planet. Sci. Lett*., 224, 509 – 527.
777  doi:10.1016/j.epsl.2004.05.035.

778  Crichton K. A., Wilson J. D., Ridgwell A., & Pearson P. N. (2021). Calibration of temperature-
779  dependent ocean microbial processes in the cGENIE.muffin (v0.9.13) Earth system model.
780  Geoscientific Model Development 14, 125-149.

781  Crosta, X., Romero, O. E., Ther, O. & Schneider, R. R. (2012). Climatically-controlled
782  siliceous productivity in the eastern Gulf of Guinea during the last 40 000 yr. *Climate of the*
783  *Past*, 8(2). 415- 431. doi:10.5194/cp-8-415-2012.

784  Crusius, J., Schroth, A. W., Gassó, S., Moy, C. M., Levy, R. C. & Gatica, M. (2011). Glacial
785  flour dust storms in the Gulf of Alaska: Hydrologic and meteorological controls and their
786  importance as a source of bioavailable iron, *Geophys. Res. Lett.,* 38, L06602.
787  doi:10.1029/2010GL046573.

788  Crusius, J., Schroth, A. W., Resing, J. A., Cullen, J., & Campbell, R. W. (2017). Seasonal and
789  spatial variabilities in northern Gulf of Alaska surface water iron concentrations driven by shelf

sediment resuspension, glacial meltwater, a Yakutat eddy, and dust. *Global Biogeochemical Cycles*, 31(6), 942-960.

de la Vega, E., Chalk, T.B., Wilson, P.A. Bysani, R. P & Foster, G. L. (2020). Atmospheric $CO_2$ during the Mid-Piacenzian Warm Period and the M2 glaciation. *Sci Rep* 10, 11002. https://doi.org/10.1038/s41598-020-67154-8.

De Schepper, S., Groeneveld, J., Naafs, B. D., Van Renterghem, C., Hennissen, J., Head, M. J., *et al.*, (2013). Northern Hemisphere Glaciation during the Globally Warm Early Late Pliocene, *PLOS ONE*, Vol. 8, Issue 12, 1-15.

DeVries T., Le Quéré C., Andrews O., Berthet S., Hauck J., Ilyina T. *et al.* (2019). Decadal trends in the ocean carbon sink. Proc Natl Acad Sci U S A. Jun 11;116(24):11646-11651. http://doi.org/10.1073/pnas.1900371116.

De Shepper, S., Groeneveld, J., Naafs, B. D., Van Renterghem, C., Hennissen, J., Head, M. J. *et al.* (2013). Northern Hemisphere Glaciation during the Glob- ally Warm Ealy Late Pliocene, PLOS ONE, 8, e81508, https://doi.org/10.1371/journal.pone.0081508.

Duk-Rodkin, A., Barendregt, R. W., Froese, D. G., Weber, F., Enkin, R., Smith, I. R., *et al.*, (2004). Timing and extent of the Plio-Pleistocene glaciations in north- western Canada and east-central Alaska, *Developments in Quaternary Sciences*, 2, 313–345.

Enkelmann, E., Koons, P. O., Pavlis, T. L., Hallet, B., Barker, A., Elliott, J., *et al.*, (2015). Cooperation among tectonic and surface processes in the St. Elias Range, Earth's highest coastal mountains, *Geophysical Research Letters*, 42 (14): 5838. doi:10.1002/2015GL064727.

Etourneau, J., Ehlert, C., Frank, M., Martinez, P., & Schneider, R. (2012). Contribution of changes in opal productivity and nutrient distribution in the coastal upwelling systems to Late Pliocene/Early Pleistocene climate cooling. *Clim. Past*, 8, 1435–1445. https://doi.org/10.5194/cp-8-1435-2012.

Fakhraee M., Planavsky N. J., & Reinhard C. T. (2020). The role of environmental factors in the long-term evolution of the marine biological pump. *Nat. Geosci.* 13, 812-816.

Galbraith, E. D., Kienast, M., Pedersen, T. F. & Calvert, S. E. (2004). Glacial- interglacial modulation of the marine nitrogen cycle by high- latitude $O_2$ supply to the global thermocline, *Paleoceanography*, 19, PA4007, doi:10.1029/ 2003PA001000.

Gallagher, S.J., Kitamura, A., Iryu, Y. Itaki, K., Koizumi, I. & Hoiles, P (2015). The Pliocene to recent history of the Kuroshio and Tsushima Currents: a multi-proxy approach. *Prog. in Earth and Planet. Sci.* 2, 17. https://doi.org/10.1186/s40645-015-0045-6.

Gaskell, S. J. & Eglinton, G., (1974). Short-term diagenesis of sterols, *Adv. Org. Geochem., Proc.* Int. Meet., 6th, Meeting Date 1973, 963-76.

Goad, L. & Withers, N. (1982). Identification of 27-nor-(24R)-24-methylcholesta- 5,22-dien-3β-ol and brassicasterol as the major sterols of the marine dinoflagellate Gymnodinium simplex, *Lipids*, 17, 853–858. doi:10.1007/bf02534578.

Gulick, S. P. S., Jaeger, J. M., Mix, A. C., Asahi, H., Bahlburg, H., Belanger, C. L., *et al.*, (2015). Mid-Pleistocene climate transition drives net mass loss from rapidly uplifting St. Elias Mountains, Alaska, *Proceedings of the National Academy of Sciences of the United States of America*, 112(49), 15042–15047. http://doi.org/10.1073/pnas.1512549112.

GEBCO Compilation Group, (2020). *GEBCO 2020 Grid*. doi:10.5285/a29c5465-b138-234d-e053-6c86abc040b9.

Hage, S., Galy, V. V., Cartigny, M. J. B., Acikalin, S., Clare, M. A., Gröcke, D. R. *et al*., (2020). Efficient preservation of young terrestrial organic carbon in sandy turbidity-current deposits. *Geology*, v. 48, p. 882–887. https:// doi.org/10.1130/G47320.1.

Hage, S., Cartigny, M. J. B., Sumner, E. J., Clare, M. A., Hughes Clarke, J. E., Talling, P. J., *et al*., (2019). Direct Monitoring Reveals Initiation of Turbidity Currents From Extremely Dilute River Plumes. *Geophysical Research Letters*, 46, 11310– 11320. https://doi.org/10.1029/2019GL084526.

Han, J. & Calvin, M. (1969). Hydrocarbon distribution of algae and bacteria, and microbiological activity in sediments. *Proceedings of the National Academy of Sciences* 64(2), 436-443. doi: 10.1073/pnas.64.2.436.

Hare, C. E., Leblanc, K., DiTullio, G. R., Kudela, R. M., Zhang, Y. Lee, P. A. *et al*. (2007). Consequences of increased temperature and $CO_2$ for phytoplankton community structure in the Bering Sea. *Mar. Ecol. Prog. Ser.*, 352, 9–16, doi:10.3354/meps07182.

Haug, G. H., Ganopolski, A., Sigman, D. M., Rosell-Melé, A., Swann, G. E. A., Tiedemann, R., *et al*. (2005). North Pacific seasonality and the glaciation of North America 2.7 million years ago. *Nature*, vol 433, 821-825.

Haug, G., Sigman, D., Tiedemann, R.,Pedersen, T. & Sarnthein, M. (1999). Onset of permanent stratification in the subarctic Pacific Ocean. *Nature*. 401. 779-782. 10.1038/44550.

Hasle, G. R., & Syvertsen, E. E. (1996). Marine Diatoms. In C. R. Tomas, *Identifying Marine Diatoms and Dinoflagellates* (pp. 5-385). San Diego, Academic Press. https://doi.org/310.1016/B1978-012693015-012693013/012650005-X.

Hedges, J. I., & Keil, R. G. (1995). Sedimentary organic matter preservation: An assessment and speculative synthesis. *Marine Chemistry*, 49 (2-3), 81–115. https://doi.org/10.1016/0304-4203(95)00008-F.

Herbert, T. D. (2001). Review of alkenone calibrations (culture, water column and sediments), *Geochem. Geophys. Geosyst*., vol 2, 2000GC000055.

Hidy, A. J., Gosse, J. C., Froese, D. G., Bond, J. D., & Rood, D. H. (2013). A latest Pliocene age for the earliest and most extensive Cordilleran Ice Sheet in northwestern Canada, *Quaternary Res.*, 61, 77–84. https://doi.org/10.1016/j.quascirev.2012.11.009.

Hinckley, S., Coyle, K.O., Gibson, G., Hermann, A.J. & Dobbins, E.L. (2009). A biophysical NPZ model with iron for the Gulf of Alaska: reproducing the differences between an oceanic HNLC ecosystem and a classical northern temperate shelf ecosystem, Deep-Sea Research II 56 (24), 2520–2536.

Horikawa, K., Martin, E., Basak, C., Onodera, J., Seki, O., Sakamoto, T., *et al*., (2015). Pliocene cooling enhanced by flow of low-salinity Bering Sea water to the Arctic Ocean. *Nature Communications* 6, 7587. https://doi.org/10.1038/ncomms8587.

Huber, B. & Bahlburg, H. (2021). The provenance signal of climate–tectonic interactions in the evolving St. Elias orogen: framework component analysis and pyroxene and epidote single grain geochemistry of sediments from IODP 341 sites U1417 and U1418. *Int J Earth Sci* (Geol Rundsch). https://doi.org/10.1007/s00531-021-02025-9.

Jaeger, J.M., Gulick, S.P.S., LeVay, L.J., Asahi, H., Bahlburg, H., Belanger, C.L., *et al*., (2014). *Proceedings of the Integrated Ocean Drilling Program*. In: Expedition reports Southern Alaska margin. Integrated Ocean Drilling Program. 341.

Joh, Y., Di Lorenzo, E., Siqueira, L. & Kirtman, B. P (2021). Enhanced interactions of Kuroshio Extension with tropical Pacific in a changing climate. *Sci Rep* 11, 6247. https://doi.org/10.1038/s41598-021-85582-y.

Kanazawa, A., Yoshioka, M. & Teshima, S.-I., (1971). The occurrence of brassicasterol in the diatoms Cyclotella nana and Nitzschia Closterium. *Bull. Jpn. Soc. Sci. Fish*. 37, 889–903.

Katsuki, K., Takahashi, K. & Okada, M. (2003). Diatom Assemblage and Productivity Changes during the Last 340,000 Years in the Subarctic Pacific. *Journal of Oceanography*, Vol. 59, pp. 695 to 707

Kiehl, J. & Trenberth, K. (1997). Earth's annual global mean energy budget. *Bulletin of the American Meteorological Society* 78, 197-208.

Kipphut, G. K. (1990). Glacial meltwater input to the Alaska Coastal Current: Evidence from oxygen isotope measurements. *Journal of Geophysical Research*, Volume 95, Issue C4.

Knudson, K. P., Ravelo, A. C., Aiello, I. W., Knudson, C. P., Drake, M. K. & Sakamoto, T. (2021). Causes and timing of recurring subarctic Pacific hypoxia. Sci. Adv.7, eabg2906.

Kornilova, O. & Rosell-Melé, A. (2003). Application of microwave-assisted extraction to the analysis of biomarker climate proxies in marine sediments. *Organic Geochemistry*, 34, 1517-1523.

Krissek, L. A. (1995). Late Cenozoic Ice-Rafting Records From Leg 145 Sites In The North Pacific: Late Miocene Onset, Late Pliocene Intensification and Pliocene-Pleistocene Events. In: Proceedings of the Ocean Drilling Scientific Results, edited by: Rea, D. K., Basov, L. A., Scholl, D. W., and Allan, J. F., Ocean Drilling Program, College Station, TX, Sci. Results, 145, 179– 194. https://doi.org/10.2973/odp.proc.sr.145.118.1995.

Lam, P. J., & Bishop, J. K. B. (2008). The continental margin is a key source of iron to the HNLC North Pacific Ocean. *Geophys. Res. Lett*., 35, doi:10.1029/2008GL033294.

Lam A.R. & Leckie R.M. (2020). Subtropical to temperate late Neogene to Quaternary planktic foraminiferal biostratigraphy across the Kuroshio Current Extension, Shatsky Rise, northwest Pacific Ocean. *PLoS ONE* 15(7): e0234351. https://doi. org/10.1371/journal.pone.0234351.

Lawrence, K. T., Herbert, T. D., Brown, C. M., Raymo, M. E. & Haywood, A. M. (2009). High-amplitude variations in North Atlantic sea surface temperature during the early Pliocene warm period. *Paleoceanography*, 24, PA2218. https://doi.org/10.1029/2008PA001669.

Lawrence, K.T., Liu, Z. & Herbert, T.D. (2006). Evolution of the eastern tropical Pacific through Plio-Pleistocene glaciation. *Science* 312, 79–83.

Lawrence, K. T., Sigman, D. M., Herbert, T. D. Riihimaki, C. A., Bolton, C. T. Martínez-Garcia A., *et al*., (2013). Time- transgressive North Atlantic productivity changes upon Northern Hemisphere glaciation. *Paleoceanography*, 28, 740–751. doi:10.1002/2013PA002546.

Lei, Y., Servais, T., Feng, Q. & He, W. (2012). The spatial (nearshore–offshore) distribution of latest Permian phytoplankton from the Yangtze Block, South China. *Palaeogeography Palaeoclimatology Palaeoecology*, 363–364:151–162. doi:10.1016/j.palaeo.2012.09.010.

Liu, Z., Altabet, M. A. & Herbert, T. D. (2008). Plio-Pleistocene denitrification in the eastern tropical North Pacific: Intensification at 2.1 Ma. *Geochem. Geophys. Geosyst*., 9, Q11006. doi:10.1029/2008GC002044.

Liu, Z., & T. D. Herbert (2004), High-latitude influence on the eastern equatorial Pacific climate in the early Pleistocene epoch, *Nature*, **427**, 720–723.

920 Liu, J., Tian, J., Liu, Z, Herbert, T. D., Fedorov, A. V. & Lyle, M (2019). Eastern equatorial
921 pacific cold tongue evolution since the late Miocene linked to extratropical climate. *Sci. Adv.* 5,
922 eaau6060.

923 Lopes, C., Kucera, M. & Mix, A. C., (2015). Climate change decouples oceanic primary and
924 export productivity and organic carbon burial. *PNAS* January 13, 2015 112 (2) 332-335.

925 Margalef, R. (1978). Life-forms of phytoplankton as survival alternatives in an unstable
926 environment. *Oceanol. Acta* 1, 493–508.

927 Marlowe, I.T., Green, J.C., Neal, A.C., Brassell, S.C., Eglinton, G. & Course, P.A. (1984).
928 Long-chain (n-$C_{37}$-$C_{39}$) alkenones in the Prymnesiophyceae. Distribution of alkenones and
929 other lipids and their taxonomic significance. *British Phycological Journal* 19, 203-216.
930 doi:10.1080/00071618400650221.

931 Martin J. H., Gordon R. M., Fitzwater S., & Broenkow W. W. (1989).
932 VERTEX: Phytoplankton/iron studies in the Gulf of Alaska. Deep-Sea Research 36: 649--680.

933 Martin, J. H. & Fitzwater, S. E. (1988). Iron deficiency limits phytoplankton growth in the
934 north-east Pacific subarctic. *Nature*, 331, 341-343

935 Martin, J. H., Michael Gordon, R. & Fitzwater, S. E., (1991). Iron limitation?. *Limnol.*
936 *Oceanogr.,* 36(8), 1793-1802.

937 Martínez-Botí, M. A., Foster, G. L. Chalk, T. B., Rohling, E. J., Sexton, P.F., Lunt, D. J., *et al*.
938 (2015). Plio-Pleistocene climate sensitivity valuated using high-resolution $CO_2$ records, Nature
939 Vol 518, issue 7537, 49-54. doi: 10.1038/nature14145.

940 Martínez-Garcia, A., Rosell-Melé, A., McClymont, E.L., Gersonde, R. & Haug, G. (2010).
941 Subpolar Link to the Emergence of the Modern Equatorial Pacific Cold Tongue. *Science*, 328,
942 1550-1553.

943 März, C., Schnetger, B. & Brumsack, H.-J. (2013). Nutrient leakage from the North Pacific to
944 the Bering Sea (IODP Site U1341) following the onset of Northern Hemispheric Glaciation?.
945 *Paleoceanography,* 28, 68–78. doi:10.1002/palo.20011.

946 Matthiessen J., Knies J., Vogt C. & Stein R. (2009). Pliocene palaeoceanography of the Arctic
947 Ocean and subarctic seas. *Phil. Trans. R. Soc. A.,* 36721–48.
948 http://doi.org/10.1098/rsta.2008.0203.

949 McGee, D., Laws, R. A. & Cahoon, L. B., Live benthic diatoms from the upper continental
950 slope: extending the limits of marine primary production, Marine Ecology Progress Series,
951 Vol. 356: 103–112 (2008), doi: 10.3354/meps07280.

952 Müller, J., Romero, O., Cowan, E. A., McClymont, E. L., Forwick, M., Asahi, H*., et al.* (2018).
953 Cordilleran ice-sheet growth fuelled primary productivity in the Gulf of Alaska, northeast
954 Pacific Ocean. *Geology.* 46 (4), pp. 307-310.

955 Müller, J., Wagner, A., Fahl, K., Stein, R., Prange, M. & Lohmann, G. (2011). Towards
956 quantitative sea ice reconstructions in the northern North Atlantic: A combined biomarker and
957 numerical modelling approach. *Earth Planet. Sci. Lett.* 306, 137–148.

958 Müller, P.J. & Schneider, R. R. (1993). An automated leaching method for the determination
959 of opal in sediments and particulate matter. *Deep-Sea Res*. I, 40, 425-444.

960 Nakov, T., Beaulieu, J.M. & Alverson, A.J. (2019). Diatoms diversify and turn over faster in
961 freshwater than marine environments. *Evolution*, 73: 2497-2511. doi:10.1111/evo.13832.

962  Palevsky, H. I., F. Ribalet, J. E. Swalwell, C. E. Cosca, E. D. Cokelet, R. A. Feely, E. V., *et*
963  *al.,* (2013). The influence of net community production and phytoplankton community
964  structure on $CO_2$ uptake in the Gulf of Alaska. *Global Biogeochem. Cycles*, 27.
965  doi:10.1002/gbc.20058.

966  Perry, S. E., Garver, J. I., & Ridway, K. D. (2009). Transport of the Yakutat Terrane, Southern
967  Alaska: Evidence from Sediment Petrology and Detrital Zircon Fission-Track and U/Pb
968  Double Dating. *The Journal of Geology*, 117, 156–173.

969  Piepho, M., Martin-Creuzburg, D. & Wacker, A., (2012). Phytoplankton sterol contents vary
970  with temperature, phosphorus and silicate supply: a study on three freshwater species.
971  *European Journal of Phycology*, 47:2, 138-145. doi: 10.1080/09670262.2012.665484.

972  Pisias, N. G., Mix, A. C. & Heusser, L, (2001). Millennial scale climate variability of the
973  Northeast Pacific Ocean and Northwest North America based on Radiolaria and pollen. *Quat.*
974  *Sci. Rev.*, 20, 1561–1576.

975  Pope, E. L., Talling, P. J. & Ó Cofaigh, C. (2018). The relationship between ice sheets and
976  submarine mass movements in the Nordic Seas during the Quaternary. *Earth-Science Reviews*
977  178, 208-256, ISSN 0012-8252. https://doi.org/10.1016/j.earscirev.2018.01.007.

978  Raja, M. & Rosell-Melé, A. (2021). Appraisal of sedimentary alkenones for the quantitative
979  reconstruction of phytoplankton biomass, *PNAS*, 118 (2), 1-7.

980  Rampen, S. W., Abbas, B. A., Schouten, S. & Sinninghe Damste, J. S. (2009). A
981  comprehensive study of sterols in marine diatoms (Bacillariophyta): Implications for their use
982  as tracers for diatom productivity. *Limnology and Oceanography*, 55. doi:
983  10.4319/lo.2010.55.1.0091.

984  Rea, D. K., Basov, I. A., Krissek, L. A. & the Leg 145 Scientific Party (1995). Scientific Results
985  of drilling the North Pacific Transect. In Rea, D. K., Basov, I. A., Scholl, D. W and Allan, J.
986  F., *Proceedings of the Ocean Drilling Program*, Scientific Results, 145.

987  Rea, D. A., & Snoeckx H. (1995). Sediment fluxes in the Gulf of Alaska; paleoceanographic
988  record from Site 887 on the Patton-Murray Seamount Platform. In Rea, D.K., Basov, LA.,
989  Scholl, D.W., and Allan, J.F. (Eds.). Proc. ODP, Sci. Results, 145: College Station, TX (Ocean
990  Drilling Program), 247-256**.**

991  Ren, J., Gersonde, R., Esper O. & Sancetta, C. (2014). Diatom distributions in northern North
992  Pacific surface sediments and their relationship to modern environmental variables.
993  *Palaeogeography, Palaeoclimatology, Palaeoecology*, 402, 81-103.
994  https://doi.org/10.1016/j.palaeo.2014.03.008.

995  Rieley G., Collier, R. J., Jones D. M. & Eglinton G. (1991). The biogeochemistry of Ellesmere
996  Lake, U.K.-I: source correlation of leaf wax inputs to the sedimentary record, *Org Geochem*
997  17, 901-912.

998  Romero, O. E., Armand, L. K., Crosta, X., & Pichon, J. J. (2005). The biogeography of major
999  diatom taxa in Southern Ocean surface sediments: 3. Tropical/Subtropical species.
1000 *Palaeogeography, Palaeoclimatology, Palaeoecology*, 223, 49-65.

1001 Romero, O. E., & Armand, L. K. (2010). Marine diatoms as indicators of modern changes in
1002 oceanographic conditions. in The Diatoms, Applications for the Environmental and Earth
1003 Sciences. 2nd ed., edited by J. P. Smol and E. F. Stoermer, pp. 373–400, Cambridge Univ.
1004 Press, Cambridge, U. K.

1005    Romero O. E. & Fischer, G. (2017). Shift in the species composition of the diatom community
1006    in the eutrophic Mauritanian coastal upwelling: Results from a multi-year sediment trap
1007    experiment (2003 – 2010). *Progress in Oceanography* 159, 31-44.

1008    Romero, O. E., Kim, J.-H., Bárcena, M. A., Hall, I. R., Zahn, R. & Schneider, R. (2015). High-
1009    latitude forcing of diatom productivity in the southern Agulhas Plateau during the past 350 kyr.
1010    *Paleoceanography* 30(2): 118-132.

1011    Romero, O. E, LeVay, L. J., McClymont, E. L., Müller, J. & Cowan, E. A. (2022). Orbital and
1012    Suborbital-Scale Variations of Productivity and Sea Surface Conditions in the Gulf of Alaska
1013    During the Past 54,000 Years: Impact of Iron Fertilization by Icebergs and Meltwater.
1014    *Paleoceanography      and      Paleoclimatology*,      37(1),      e2021PA004385,
1015    https://doi.org/10.1029/2021PA004385.

1016    Romero, O.E., Mohtadi, M., Helmke, P. & Hebbeln, D. (2012). High Interglacial Diatom
1017    Paleoproductivity in the Westernmost Indo-Pacific Warm Pool During the Past 130,000 yr.
1018    *Paleoceanography* 27, PA3209.

1019    Romero, O. E., Ramondenc, S., & Fischer, G. (2021). A 2-decade (1988–2009) record of
1020    diatom fluxes in the Mauritanian coastal upwelling: impact of low-frequency forcing and a
1021    two-step shift in the species composition. *Biogeosciences* 18(5): 1873-1891.

1022    Romero, O. E., Rixen, T., & Herunadi, B. (2009). Effects of hydrographic and climatic forcing
1023    on diatom production and export in the tropical southeastern Indian Ocean. *Marine Ecology
1024    Progress Series* 384: 69-82.

1025    Sagredo, E., A., Rupper, S. & Lowell, T. V. (2014). Sensitivies of the equilibrium line altitude
1026    to temperature and precipitation changes along the Andes. *Quaternary Research* 81 (2), 355-
1027    366. https://doi.org/10.1016/j.yqres.2014.01.008.

1028    Sancetta, C. (1981). Oceanographic and ecologic significance of diatoms in surface sediments
1029    of the Bering and Okhotsk seas. Deep-Sea Research, 28 (1981), pp. 789-817.

1030    Sancetta, C., & Calvert, S. E., (1988). The annual cycle of sedimentation in Saanich inlet,
1031    British Columbia: implications for the interpretation of diatom fossil assemblages. *Deep Sea
1032    Research Part A. Oceanographic Research Papers*, Volume 35, Issue 1, 1988, Pages 71-90,
1033    ISSN 0198-0149, https://doi.org/10.1016/0198-0149(88)90058-1.

1034    Sancetta, C., & Silvestri, S.M. (1986). Pliocene-Pleistocene evolution of the North Pacific
1035    ocean-atmospheric system, interpreted from fossil diatoms. *Paleoceanography*, volume 1,
1036    Number 2, Pages 163-180.

1037    Sánchez-Montes, M. L., McClymont, E. L., Lloyd, J. M., Müller, J., Cowan, E. A. & Zorzi, C.
1038    (2019). Alkenone sea surface temperatures, ice rafted debris, terrestrial/aquatic n-alkane ratio,
1039    pollen counts and a new age and depth models from IODP Expedition 341 Site U1417, Gulf
1040    of Alaska. *PANGAEA*. https://doi.org/10.1594/PANGAEA.899064.

1041    Sánchez-Montes, M. L., McClymont, E. L., Lloyd, J. M., Müller, J., Cowan, E. A. & Zorzi, C.
1042    (2020). Late Pliocene Cordilleran Ice Sheet development with warm northeast Pacific sea
1043    surface temperatures, *Clim. Past*, 16, 299–313, https://doi.org/10.5194/cp-16-299-2020.

1044    Sánchez-Montes, M. L., Romero, O. E., Cowan, E. A., Müller, J., Moy, C. M., Lloyd, J. M. *et
1045    al.* (2021). Lipid biomarkers, siliceous microfossil assemblages, biogenic silica and carbon and
1046    nitrogen bulk and isotope analyses from IODP Hole 341-U1417D, Gulf of Alaska. *PANGAEA*.
1047    https://doi.pangaea.de/10.1594/PANGAEA.936779.

1048  Schrader, H. & Gersonde, R. (1978). Diatoms and silicoflagellates. In Zachariasse etb al. Microplaeontological counting methods and techniques - an excercise on an eight metres section of the lower Pliocene of Capo Rossello. Sicily. *Utrecht Micropal. Bull.* 17, pp. 129-176.

1052  Seki, O., Foster, G. J., Schmidt, D. N., Mackensen, A., Kawamura, K. & Pancost, R. D. (2010). Alkenone and boron-based Pliocene $pCO_2$ records, Earth and Planetary Science Letters 292, 201-211. doi:10.1016/j.epsl.2010.01.037.

1055  Shannon, C. E. & Weaver, W. (1949). The Mathematical Theory of Communication. *Urbana: University of Illinois Press*.

1057  Shimada, C., Sato, T., Yamasaki, M., Hasegawa, S. & Tanaka, Y., (2009). Drastic change in the late Pliocene subarctic Pacific diatom community associated with the onset of the Northern Hemisphere Glaciation, *Palaeogeography, Palaeoclimatology, Palaeoecology*, 279 (3-4), 207-215. https://doi.org/10.1016/j.palaeo.2009.05.015.

1061  Sigman, D. M., Jaccard, S. L. & Haug, G. H. (2004). Polar ocean stratification in a cold climate. *Nature,* 428, 59–63.

1063  Schlitzer, R. (2016). Ocean Data View. http://odv.awi.de.

1064  Schroth, A. W., Crusius, J., Gassó, S., Moy, C. M., Buck, N. J., Resing, J. A., *et al.* (2017). Atmospheric deposition of glacial iron in the Gulf of Alaska impacted by the position of the Aleutian Low. Geophysical research letters, 44(10), 5053–5061. https://doi.org/10.1002/2017gl073565.

1068  Stockwell, D. A., Whitledge, T. E, Zeeman, S. I., Coyle, K. O., Napp, J. M., Brodeur, R. D. *et al.* (2001). Anomalous conditions in the south-eastern Bering Sea, 1997: Nutrients, phytoplankton and zooplankton. *Fish. Oceanogr.*, **10**, 99–116, doi:10.1046/j.1365-2419.2001.00158.x.

1072  Studer, A. S., Martínez-Garcia, A., Jaccard, S. L., Girault, F. E., Sigman, D. M. & Haug. G. H. (2012). Enhanced stratification and seasonality in the Subarctic Pacific upon Northern Hemisphere Glaciation–New evidence from diatom-bound nitrogen isotopes, alkenones and archaeal tetraethers. *Earth and Planetary Science Letters*, 351–352, 84-94, ISSN 0012-821X. https://doi.org/10.1016/j.epsl.2012.07.029.

1077  Swann, G. E. A., Maslin, M. A., Leng, M. J., Sloane, H. J., & Haug, G. H. (2006). Diatom $\delta^{18}O$ evidence for the development of the modern halocline system in the subarctic northwest Pacific at the onset of major Northern Hemisphere glaciation, Paleoceanography, 21, PA1009. doi:10.1029/2005PA001147.

1081  Talling, P. J., Baker, M., Pope, E., Cula, C. A., Cartigny, M., Faria, R., *et al.*, (2021). Novel sensor array helps to understand submarine cable faults off West Africa. *Earth ArXiv*. https://doi.org/10.31223/X5W328.

1084  Thunell, R. C., Pride, C. J., Tappa, E. & Muller-Karger, F. E. (1994). Biogenic silica fluxes and accumulation rates in the Gulf of California. *Geology* 22 (4): 303–306. doi: https://doi.org/10.1130/0091-7613(1994)022<0303:BSFAAR>2.3.CO;2.

1087  Tsuda, A., Takeda, S., Saito, H., Nishioka, J., Nojiri, Y., Kudo, I., *et al.*, (2003). A mesoscale iron enrichment in the western subarctic Pacific induces a large centric diatom bloom. *Science* 300, 958–961.

1090 USGS (U.S. Geological Survey) (1981). Geographic Names Phase I data compilation (1976-
1091 1981). *Geographic Names Information System,* https://edits.nationalmap.gov/apps/gaz-
1092 domestic/public/summary/1413097, last accessed 06-03-2022.

1093 Verardo, D.J., Froelich, P.N. & McIntyre, A. (1990). Determination of organic carbon and
1094 nitrogen in marine sediments using the Carlo Erba NA-1500. *Deep-Sea Research, Part I
1095 (Oceanographic Research Papers)* 37, 157-165.

1096 Volkman, J. K. (1986). A review of sterol markers for marine and terrigenous organic matter.
1097 *Org. Geochem.,* 9, 83–99.

1098 Volkman, J.K. (2006). Lipid markers for marine organic matter. In: Volkman, J.K. (Ed.),
1099 Handbook of Environmental Chemistry, vol. 2. Springer-Verlag, Berlin, Heidelberg, pp. 27–
1100 70.

1101 Wakeham, S.G., Peterson, M.L., Hedges, J.I. & Lee, C. (2002). Lipid biomarker fluxes in the
1102 Arabian Sea, with a comparison to the equatorial Pacific Ocean. *Deep-Sea Research*, Part 2,
1103 Topical Studies in Oceanography 49 (12), 2265 – 2301.

1104 Walton, M. A. L., Gulick, S. P. S, Reece, R. S., Barth, G. A., Christeson, G. L. & Van
1105 Avendonk, H. J. A. (2014). Dynamic response to strike-slip tectonic control on the deposition
1106 and evolution of the Baranof Fan, Gulf of Alaska. *Geosphere*; v. 10, no. 4, p. 680–691.
1107 doi:10.1130/GES01034.1.

1108 Wang J, Chang F, Li T, Sun H, Cui Y & Liu T. (2020). The evolution of the Kuroshio Current
1109 over the last 5 million years since the Pliocene: Evidence from planktonic foraminiferal faunas.
1110 *Science China Earth Sciences*, 63(11): 1714–1729. https://doi.org/10.1007/s11430-019-9641-
1111 9.

1112 Wang, K.J., Huang, Y., Majaneva, M., Belt, S. T., Liao, S., Novak, J. *et al*., (2021). Group 2i
1113 Isochrysidales produce characteristic alkenones reflecting sea ice distribution. *Nature
1114 Communications* 12, 15. https://doi.org/10.1038/s41467-020-20187-z.

1115 Walinsky, S. E., Prahl, F. G., Mix, A. C., Finney, B. P., Jaeger, J. M. & Rosen, G. P. (2009).
1116 Distribution and composition of organic matter in surface sediments of coastal southeast
1117 Alaska, Cont. Shelf Res., 29(13), 1565–1579. doi:10.1016/j.csr.2009.04.006.

1118 Weingartner, T. (2007). Chapter 2.2: The physical environment of the Gulf of Alaska. In: Spies,
1119 R.B. (Ed.), Long-term Ecological Change in the Northern Gulf of Alaska. *Elsevier*, Oxford, p.
1120 589.

1121 Whitney, F. A., Crawford, D. W. & Yoshimura, T. (2005). The uptake and export of silicon
1122 and nitrogen in HNLC waters of the NE Pacific Ocean. *Deep Sea Res*., Part II, 52(7–8), 1055–
1123 1067. doi:10.1016/j.dsr2.2005.02.006.

1124 Williamson, P. & Holligan, P. M. (1990). Ocean productivity and climate change. *Trends in
1125 Ecology and Evolution* 5, 9, 299-303

1126 Zdanowicz, C., Hall, G., Vaive, J., Amelin, Y., Percival, J., Girard, I. *et al*. (2006). Asian dust
1127 fall in the St. Elias Mountains, Yukon, Canada Geochim. Cosmochim. Acta, 70, pp. 3493-
1128 3507.

1129 Zindorf, M., März, C., Wagner, T., Gulick, S. P. S., Strauss, H., Benowitz, J., *et al*., (2019).
1130 Deep Sulfate-Methane-Transition and sediment diagenesis in the Gulf of Alaska (IODP Site
1131 U1417). Marine Geology, 417, 105986. https://doi.org/10.1016/j.margeo.2019.105986.

1132  Zindorf M, Rush D, Jaeger J, Mix A, Penkrot ML, Schnetger B, *et al*., (2020). Reconstructing
1133  oxygen deficiency in the glacial Gulf of Alaska: Combining biomarkers and trace metals as
1134  paleo-redox proxies, Chemical Geology, 558. https://doi.org/10.1016/j.chemgeo.2020.119864.
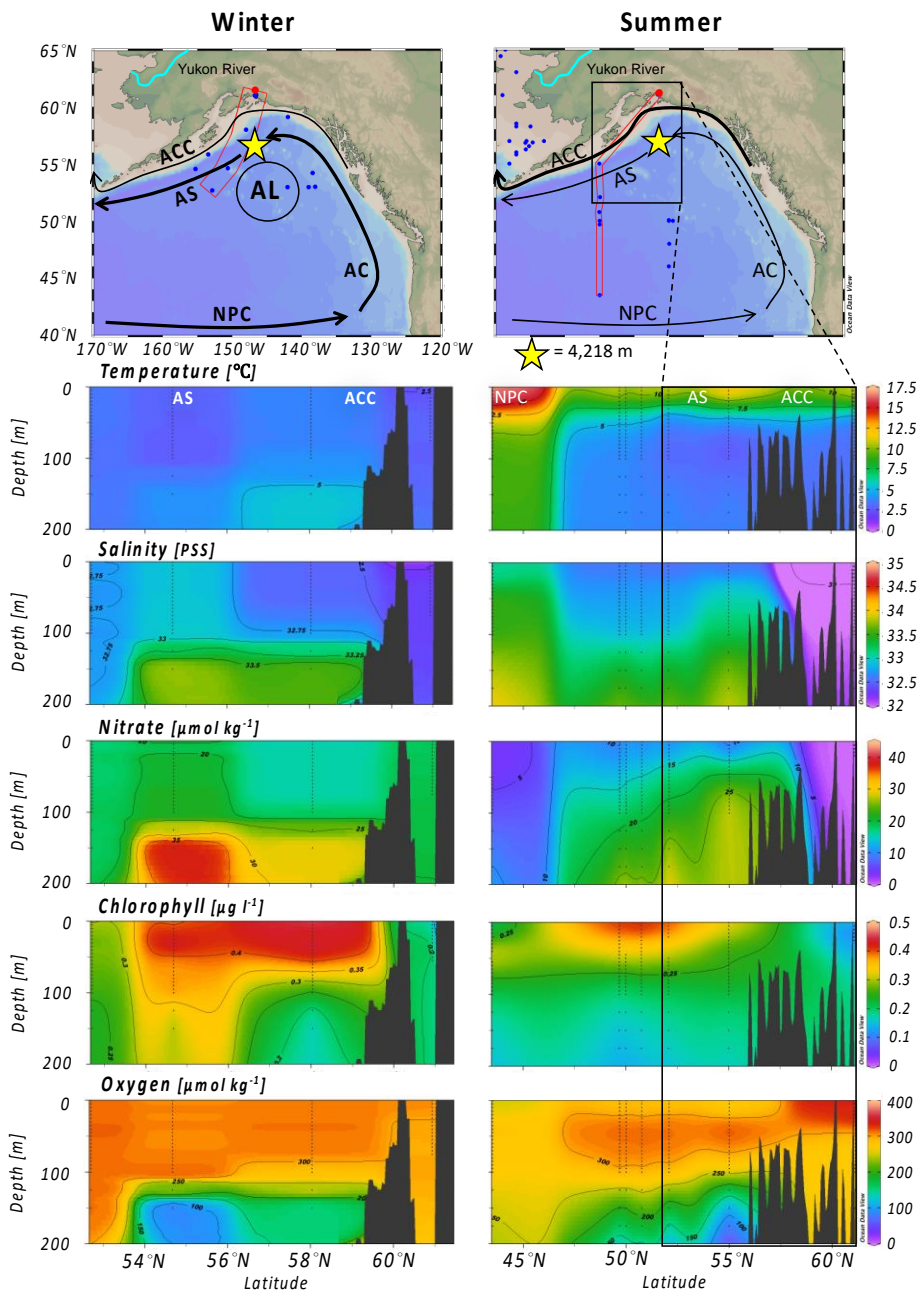
1135

**Figure 1:** Modern ocean currents and onshore to offshore water properties in the GOA. Map
of the GOA showing data collection sites (blue dots) and selected transect (red rectangle, upper
panels) that give rise to the vertical plots; temperature (ºC) salinity (pps), nitrate (μmol kg$^{-1}$),
chlorophyll (μgl l$^{-1}$) and oxygen (μmol kg$^{-1}$) during winter (F-M, left) and summer (J-A-S,
right). ACC=Alaska Coastal Current, AC=Alaska Current, AS= Alaska Stream, NPC=North
Pacific Current, AL=Aleutian Low. The location of site U1417 is indicated with yellow stars
and the River Yukon is represented in blue in the upper panels. Data downloaded from World
Ocean Database (Boyer *et al*., 2013), bathymetry data downloaded from GEBCO (GEBCO,
2020) and plotted with Ocean Data View (Schlitzer, 2016). The CIS would occupy the highest

1145    Alaskan topography (darker brown colours) of Wrangell-St. Elias and McKenzie Mountains,
1146    partially the Yukon and Tanana upland and Olgivine Mountains during the Pliocene-early
1147    Pleistocene (2.9-2.6 Ma, Duk-Rodkin *et al.*, 2004).
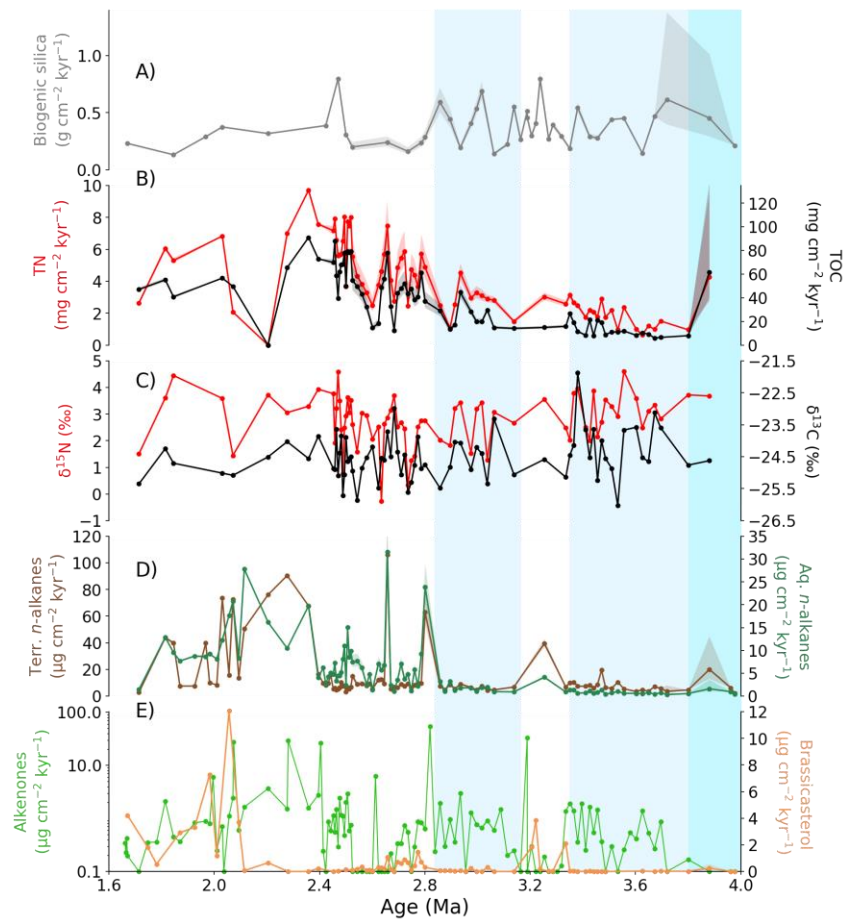


1148

1149    **Figure 2**: Terrestrial and marine productivity bulk and biomarker results at Site U1417. **a)**
1150    Biogenic silica MAR (g cm$^{-2}$ kyr$^{-1}$), **b)** total nitrogen (mg cm$^{-2}$ kyr$^{-1}$, red) and total organic
1151    carbon MAR (mg cm$^{-2}$ kyr$^{-1}$, black) and **c)** $\delta^{15}$N (‰, red) and $\delta^{13}$C (‰, black); **d)** Terrestrial
1152    (brown, left) and aquatic (turquoise, right) n-alkanes MAR (μ g cm$^{-2}$ kyr$^{-1}$) and **e)** alkenone
1153    (green, left) and brassicasterol MAR (orange, right) (μ g cm$^{-2}$ kyr$^{-1}$). Shadings indicate
1154    uncertainties in MAR associated with the age and depth uncertainties of the tie-points in Jaeger
1155    *et al.* (2014) and age-depth adjustments in Sánchez-Montes *et al.* (2020).
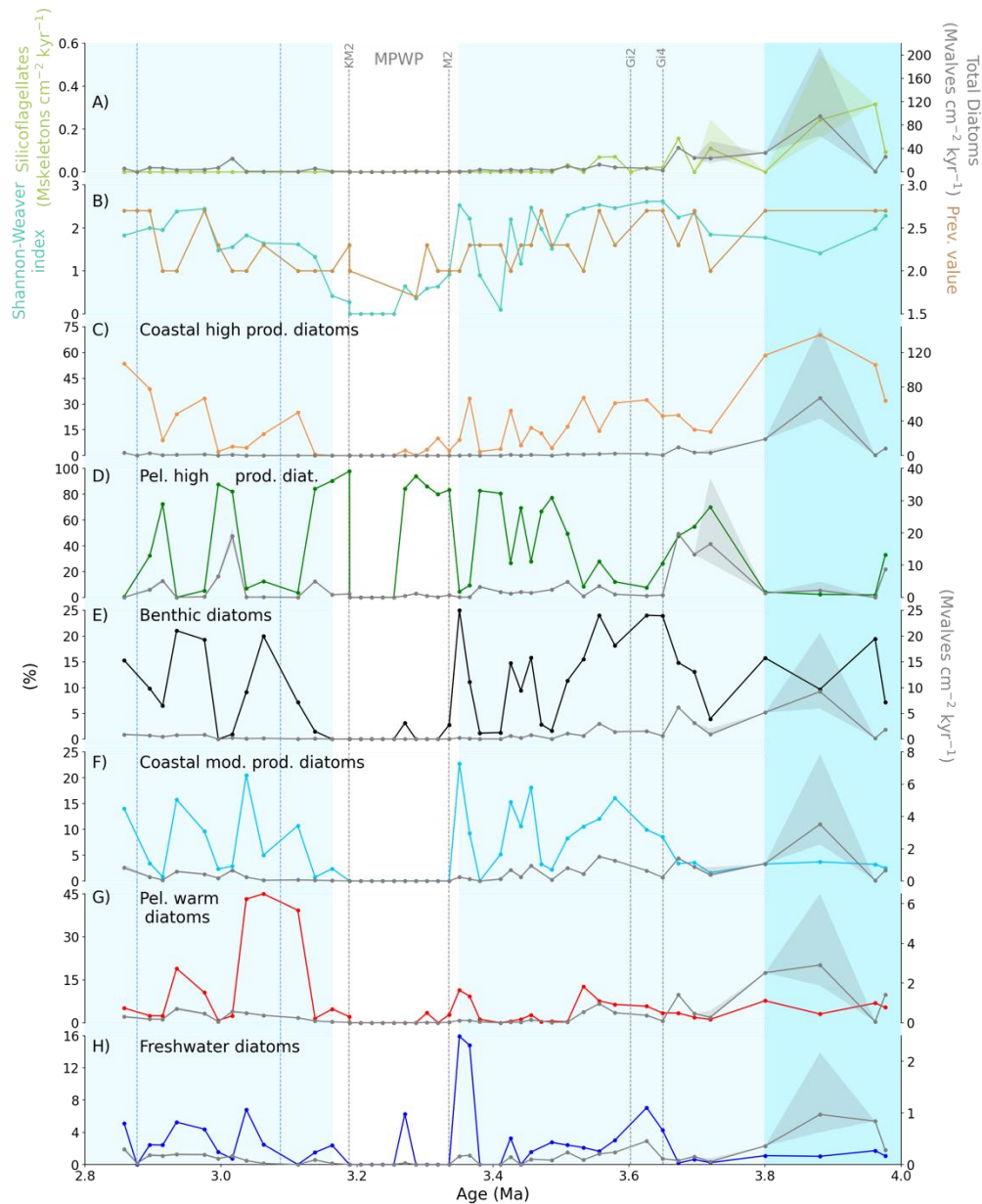
**Figure 3:** Detailed Pliocene (4.0-2.8 Ma) marine productivity export at Site U1417. **a)** Silicoflagellate MAR (million skeletons cm$^{-2}$ kyr$^{-1}$, green) and total diatom MAR (million valves cm$^{-2}$ kyr$^{-1}$, grey); **b)** the Shannon-Weaver index of diversity of species (turquoise) and the preservation value (brown); **c)** coastal high productivity diatom species relative abundance (%; orange) and MAR (million valves cm$^{-2}$ kyr$^{-1}$, grey); **d)** pelagic high productivity diatom species relative abundance (%; green) and MAR (million valves cm$^{-2}$ kyr$^{-1}$, grey); **e)** benthic diatom species relative abundance (%; in black) and MAR (million valves cm$^{-2}$ kyr$^{-1}$, grey); **f)** coastal moderate productivity diatom species relative abundance (%; in blue) and MAR (million valves cm$^{-2}$ kyr$^{-1}$, grey); **g)** pelagic warm diatom species relative abundance (%; in red) and MAR (million valves cm$^{-2}$ kyr$^{-1}$, grey) and **h)** freshwater diatoms relative abundance (%, blue) and MAR (million valves cm$^{-2}$ kyr$^{-1}$, grey). Vertical lines correspond to glacial stages (grey) and key events on the CIS runoff history (blue, see text). Blue vertical shadings indicate higher (deeper blue) and high (light blue) biogenic silica preservation, the non-shaded interval indicates poor silica preservation. Shadings indicate uncertainties in MAR associated with the age and depth uncertainties of the tie-points in Jaeger *et al*. (2014) and age-depth adjustments in Sánchez-Montes *et al*. (2020).
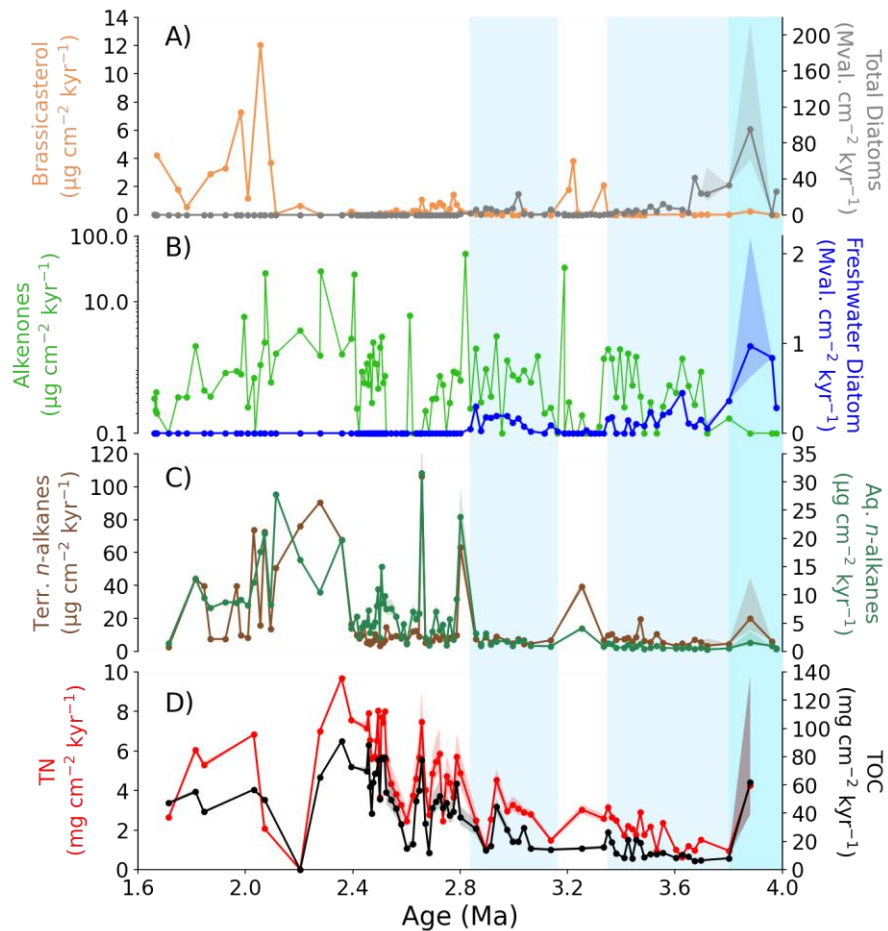
1173



1174 **Figure 4:** Plio-Pleistocene productivity export and water column ventilation. **a)** total diatom
1175 MAR (million valves cm$^{-2}$ kyr$^{-1}$;grey) and brassicasterol MAR (μg cm$^{-2}$ kyr$^{-1}$; orange); **b)**
1176 freshwater diatom MAR (blue, million valves cm$^{-2}$ kyr$^{-1}$; blue) and alkenone MAR (μg cm$^{-2}$
1177 kyr$^{-1}$; light green) in log scale; **c)** terrigenous (brown) and aquatic (turquoise) n-alkane MAR
1178 (μg cm$^{-2}$ kyr$^{-1}$) and **d)** total nitrogen (TN; red) MAR (mg cm$^{-2}$ kyr$^{-1}$) and total organic carbon
1179 (TOC; black) at Site U1417 against age (Ma). Blue vertical shadings indicate higher (deeper
1180 blue) and high (light blue) biogenic silica preservation, the rest non-shaded intervals indicate
1181 increases in organic matter (OM) preservation (e.g. the MPWP (3.33-3.19 Ma)). Shadings
1182 indicate uncertainties in MAR associated with the age and depth uncertainties of the tie-points
1183 in Jaeger *et al*. (2014) and age-depth adjustments in Sánchez-Montes *et al*. (2020).
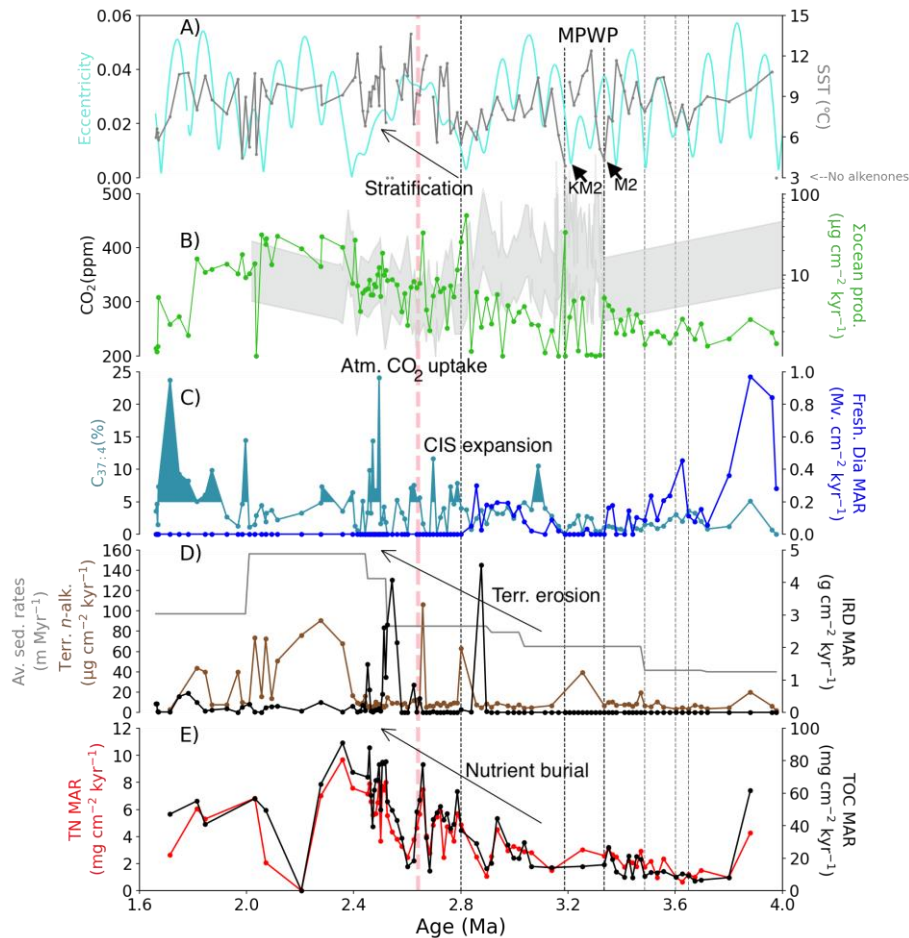
1184

**Figure 5:** The development of the North Pacific stratification and the nitrogen and carbon cycling. **a)** Earth's eccentricity reconstruction (light blue; Berger and Loutre, 1999) and $U^{K}_{37}$' SST (°C) at Site U1417 (grey; Sánchez-Montes *et al*., 2019); **b)** atmospheric $CO_2$ upper- and lower-end (ppm) estimates on the Caribbean Sea based on alkenone $\delta^{13}C$ (Site ODP 999A; Seki *et al*., 2010b) and marine $\delta^{11}B$ (Site ODP 999; Martínez-Botí *et al.,* 2015; de la Vega *et al.,* 2020) (grey) and sum of ocean productivity proxies (alkenone, brassicasterol and aquatic *n*-alkane MAR, μg cm$^{-2}$ kyr$^{-1}$, light green) in log scale; **c)** $C_{37:4}$ (%) as a record of meltwater inputs (turquoise, Sánchez-Montes *et al.,* 2019) and freshwater diatom MAR (blue, million valves cm$^{-2}$ kyr$^{-1}$, blue); **d)** and terrigenous (brown) n-alkane MAR (μg cm$^{-2}$ kyr$^{-1}$), average sedimentation rates at U1417 (m Myr$^{-1}$; Sánchez-Montes *et al.,* 2019) and IRD MAR (g cm$^{-2}$ kyr$^{-1}$; Sánchez-Montes *et al*., 2019; black); **e)** total nitrogen (TN; red) MAR (mg cm$^{-2}$ kyr$^{-1}$) and total organic carbon (TOC; black) at Site U1417 vs age in million years before present (Ma; Sánchez-Montes *et al*., 2019). Grey dashed vertical lines indicate the timing of the Gi4, Gi2 and disappearance of silicoflagellates (see Figure 3). Black dashed lines indicate the timing of the M2, KM2, which capsulate the MPWP, and the start of the iCIS. Pink vertical dashed line indicates the maximum extension of the CIS at the lower Klondike Valley, Yukon interior (2.64 Ma; Hidy *et al*., 2013). Black arrows highlight the tendency of the proxies at key intervals.
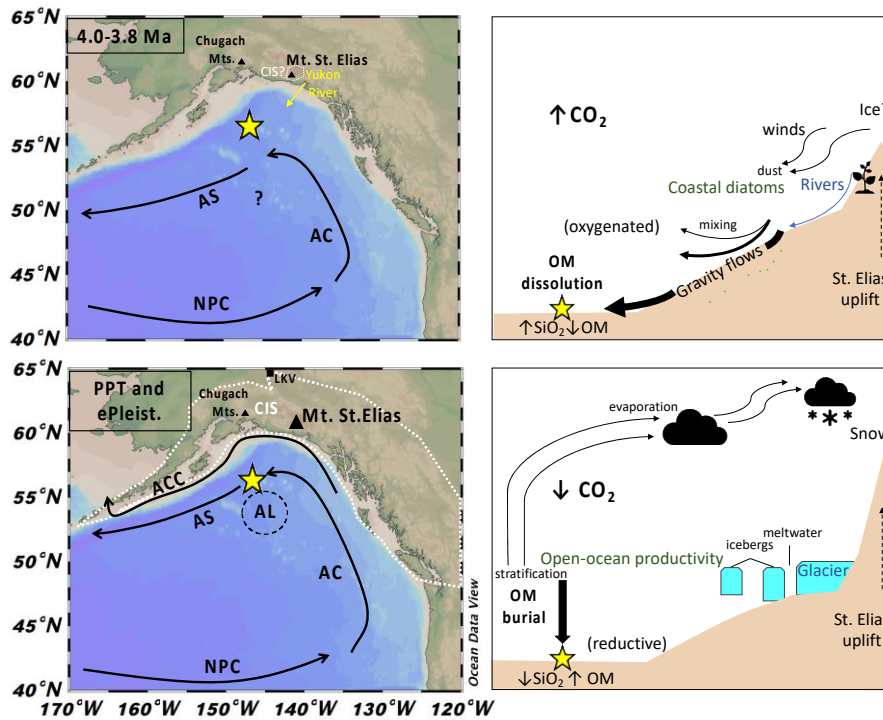
1203

**Figure 6**: Schematic overview of the Plio-Pleistocene changes in the GOA's atmosphere and
ocean circulation. **Left)** Schematic circulation over a modern map of the GOA with similar
labels as in Figure 1 (Ocean Data View; Schlitzer, 2016) and **right)** Alaskan coast to Site
U1417 transect simplifying the water column characteristics discussed in the text during the
**top)** early Pliocene (4.0-3.8 Ma) and **bottom)** the Plio-Pleistocene Transision (PPT) and early
Pleistocene. The top left panel indicates a weaker and possibly different ocean circulation than
at present, and the Yukon River Basin runoff during the Pliocene (yellow arrow; Duk-Rodkin
*et al.,* 2004) and possible CIS extension (interpreted from Enkelmann *et al.,* 2015; white dashed
line) and smaller St. Elias Mountain altitude (interpreted from Enkelmann *et al.*, 2015; black
triangles). The bottom left panel indicates the CIS Pliocene-early Pleistocene maximum
extension (Duk-Rodkin *et al.,* 2004; Hidy *et al.*, 2013; white dashed line; LKV=Lower
Klondike Valley) and higher Mt. St. Elias altitude (>2,000 m, Duk Rodkin et al., 2004).
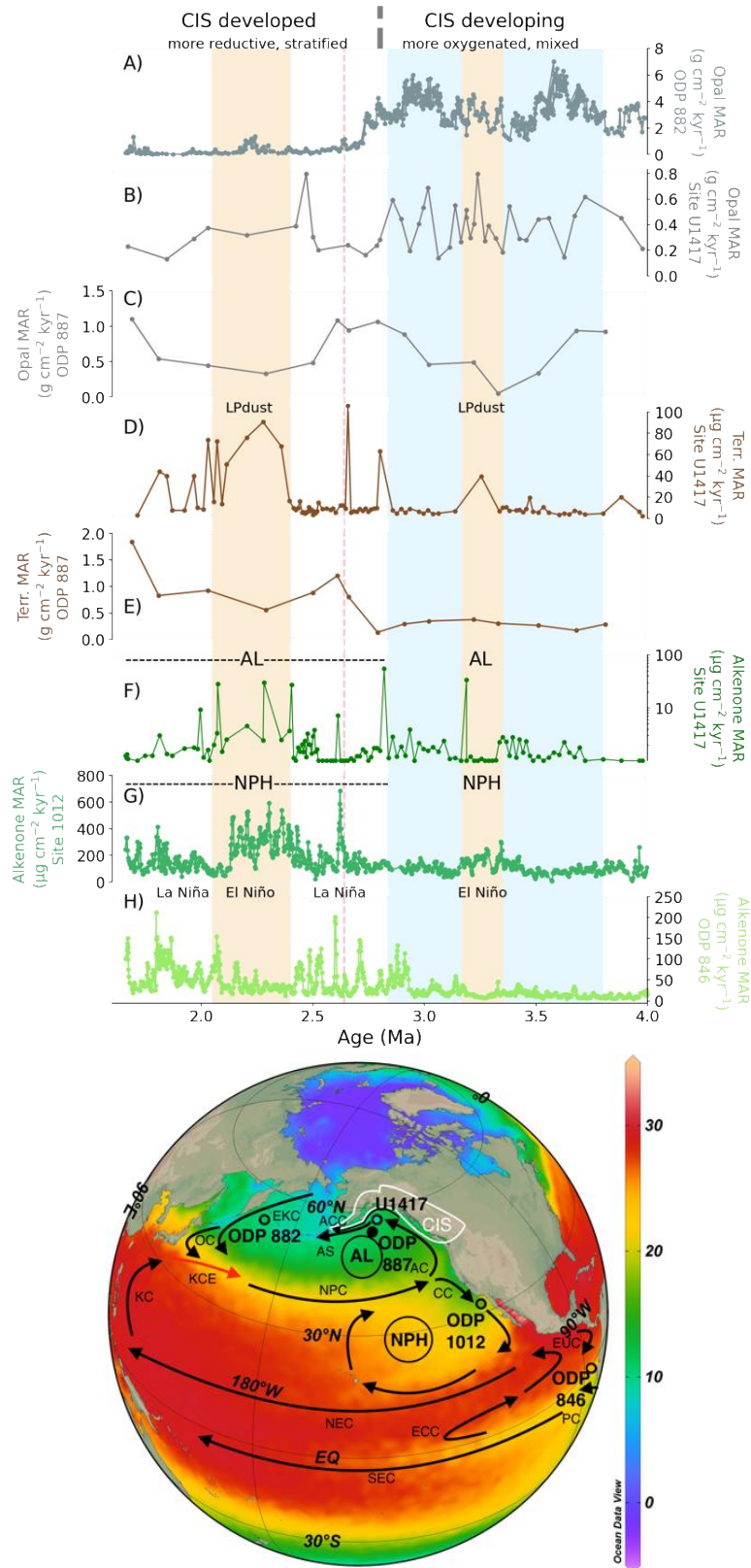
**Figure 7:** Productivity and ocean circulation in the north Pacific. **Upper panel: a)** ODP 882 biogenic silica MAR (g cm⁻² kyr⁻¹) located in the subarctic west (Haug *et al.* 1999), **b)** Site U1417 biogenic silica MAR (g cm⁻² kyr⁻¹), **c)** ODP 887 biogenic silica MAR (g cm⁻² kyr⁻¹), located 200 km southwest of U1417 (Rea & Snoeckx, 1995), **d)** Site U1417 terrigenous *n*-alkane MAR (µg cm⁻² kyr⁻¹), **e)** ODP 887 total terrigenous MAR (g cm⁻² kyr⁻¹) (Rea & Snoeckx,

1222   1995), **f)** Site U1417 alkenone MAR ($\mu$g cm$^{-2}$ kyr$^{-1}$), **g)** Site U1012 alkenone MAR ($\mu$g cm$^{-2}$
1223   kyr$^{-1}$), located in the east Cortez Basin, 100 km southwest of San Diego (Liu *et al.* 2008) and
1224   **h)** ODP 846 alkenone MAR ($\mu$g cm$^{-2}$ kyr$^{-1}$), in the equatorial east Pacific (Liu & Herbert, 2004)
1225   where references to La Niña and El Niño refer to La Niña and El Niño-like conditions. Blue
1226   vertical shadings indicate the transitional water columns across more oxygenated (4.0-3.8 Ma)
1227   to more reductive (3.3-3.2 Ma, MPWP) and from the more reductive MPWP through more
1228   oxygenated (3.2-2.82 Ma) to more reductive (2.8-1.66 Ma). Pink vertical dashed line indicates
1229   the maximum extension of the CIS at the lower Klondike Valley, Yukon interior (2.64 Ma;
1230   Hidy *et al.*, 2013). Orange shadings indicate higher terrestrial *n*-alkanes from the Loess Plateau
1231   and higher alkenone MAR at Site U1417 and Site 1012, associated with El Niño. **Lower panel:**
1232   Pacific globe view with modern ocean circulation (Ocean Data View; Schlitzer, 2016), summer
1233   SSTs (September 1955– 2013, NOAA WOA13; Locarnini *et al.,* 2013) and location of drilling
1234   sites shown in the upper panel circle-coloured with the early Pleistocene SST average, which
1235   depict North Pacific SST gradients similarly to the negative PDO (discussed in Sánchez-
1236   Montes *et al.*, 2020; black filling at ODP 887 indicates no data). PC=Peru Current, SEC= South
1237   Equatorial Current, ECC= Equatorial Countercurrent, EUC=Equatorial Undercurrent, NEC=
1238   North Equatorial Current, EKC=East Kamchatka Current, OC=Oyashio Current, KC=Kurosio
1239   Current, KCE=Kuroshio Current Extension, NPC=North Pacific Current, AC=Alaska Current,
1240   ACC=Alaska Coastal Current, AS=Alaska Stream and CC=California Current.
1241   CIS=Cordilleran Ice Sheet extent (early Pleistocene maximum extension, Duk-Rodkin *et al.*,
1242   2004; Hidy *et al.*, 2013; white line), AL=Aleutian Low and NPH=North Pacific High.